A DETAILED LOOK AT THE OMEGA-K ALGORITHM FOR PROCESSING SYNTHETIC APERTURE RADAR DATA

by

Matthew A. Tolman

A thesis submitted to the faculty of

Brigham Young University

in partial fulfillment of the requirements for the degree of

Master of Science

Department of Electrical and Computer Engineering

Brigham Young University

December 2008

BRIGHAM YOUNG UNIVERSITY

GRADUATE COMMITTEE APPROVAL

of a thesis submitted by

Matthew A. Tolman

This thesis has been read by each member of the following graduate committee and by majority vote has been found to be satisfactory.

Date	David G. Long, Chair
Date	Brian D. Jeffs
Date	Karl F. Warnick

BRIGHAM YOUNG UNIVERSITY

As chair of the candidate's graduate committee, I have read the thesis of Matthew A. Tolman in its final form and have found that (1) its format, citations, and bibliographical style are consistent and acceptable and fulfill university and department style requirements; (2) its illustrative materials including figures, tables, and charts are in place; and (3) the final manuscript is satisfactory to the graduate committee and is ready for submission to the university library.

Date

David G. Long
Chair, Graduate Committee

Accepted for the Department

Michael J. Wirthlin
Graduate Coordinator

Accepted for the College

Alan R. Parkinson
Dean, Ira A. Fulton College of
Engineering and Technology

ABSTRACT

A DETAILED LOOK AT THE OMEGA-K ALGORITHM FOR PROCESSING SYNTHETIC APERTURE RADAR DATA

Matthew A. Tolman

Department of Electrical and Computer Engineering

Master of Science

In this thesis, the Omega-k algorithm used for processing stripmap synthetic aperture radar (SAR) data is explored in detail. While the original Omega-k algorithm does not achieve the same SNR as a matched filter, a modification is presented which enables the algorithm to nearly achieve that SNR. It is shown that the focused point spread function obtained when the Omega-k algorithm is used differs in important ways from the output of a modified version of the matched filter. Spread out sidelobes and a stretched mainlobe are observed when the data is processed by the Omega-k algorithm. These differences may increase the potential interference between some nearby scatterers; however, the amplitude of the resulting sidelobes is lower than that observed for the matched filter, and the potential interference between other nearby scatterers is reduced.

The details of a discrete implementation of the algorithm are also presented. Two methods for mixing the frequency domain signal to baseband are compared, and one is shown to potentially reduce the required accuracy of the interpolation kernel.

Finally, the errors associated with the key approximation used by the algorithm are explored through simulation, and it is shown that the approximation is sufficiently accurate for a particularly demanding configuration.

ACKNOWLEDGMENTS

First, I must acknowledge my advisor Dr. Long who has helped me to develop a broader perspective when approaching problems and has gone out of his way many times to revise this thesis. In addition to Dr. Long, I thank my wife for her unfailing support throughout the entire process.

Table of Contents

List of Tables

List of Figures

Chapter 1

Introduction

Synthetic aperture radar (SAR) systems are imaging radar systems which are capable of producing both two- and three-dimensional images of an area [1] [2] [3]. While SAR was developed and used by the military decades earlier, the launch of the SEASAT satellite in 1978 was an important step towards its use by the wider remote sensing community [1]. During the 1990's, increased interest resulted in a number of satellites being equipped with SAR sensors [1].

Here at BYU, emphasis has been placed on producing light-weight, low-cost SAR systems to be flown on small aircraft. Pursuit of this goal has progressed through a number of system designs which include: the YSAR [4], the YINSAR [5], the microSAR [6], the microASAR, and the nuSAR. Along with the design and implementation of the hardware for these systems, significant work has gone into developing and testing various processing algorithms for possible implementation.

1.1 Thesis Context

Many processing algorithms exist to process SAR data. The standard algorithms are the range-Doppler algorithm (RDA) [1], the chirp scaling algorithm (CSA) [1], and the Omega-k algorithm [7]. Comparisons of these algorithms have been performed in the past [8] [9] [10] [11]; however, they have focused on evaluating the resulting frequency domain phase not the resulting time-domain signal. In [10], the point spread function is considered but only for an approximate version of the Omega-k algorithm. In [11], the Omega-k algorithm is considered optimal and is used as the reference to which other algorithms are compared.

The purpose of this thesis is to extend the analysis performed by others to analyze the point spread function output by the Omega-k algorithm, and to explore some additional aspects of the Omega-k algorithm. The topics covered include: identifying the portion of the processed image which represents properly focused data, exploring the effect of the Stolt mapping (a key aspect of the algorithm) on the focused point spread function, comparing the peak SNR achieved by the algorithm to that of an ideal matched filter, developing a discrete implementation of the algorithm, and understanding the effect of the POSP approximation errors.

This thesis contributes to the work already done in primarily two ways. First, the effect of the frequency domain mapping employed by the Omega-k algorithm on the resulting point-spread function is explored both analytically and through simulation. Second, the magnitude and the effect of the POSP approximation errors are explored. This analysis addresses the effect of the associated frequency domain phase errors on the resulting point spread function. In all of this work, the analytical development provides insight into how the results of the simulation may be extended to other SAR systems.

1.2 Thesis Outline

The rest of the thesis is organized into five chapters.

In Chapter 2, the basic principles of radar and the geometry associated with stripmap SAR systems are used to develop the equation for the SAR signal. The frequency domain expression for the SAR signal obtained using the POSP approximation is also discussed.

In Chapter 3, the effect of choosing a particular amount of time to collect the radar echos is discussed, and the equations for identifying pixels which represent properly processed data are developed.

In Chapter 4, the Omega-k algorithm is presented and is compared to the output of an ideal matched filter for a single target. The required modification to achieve an SNR nearly equivalent to the matched filter is discussed, and the effect of the frequency domain mapping is explored through simulation.

In Chapter 5, the issues associated with a discrete implementation of the algorithm are presented, and two methods for ensuring that the frequency domain signal is properly mixed to baseband are compared.

In Chapter 6, the POSP approximation is analyzed and the effects of the frequency domain phase errors are explored through simulation.

Chapter 2

The SAR Signal

Synthetic aperture radars are commonly used to produce two or three dimensional images of the earth's surface. The mathematical relationship between the received data and the desired image is often developed through the use of Doppler frequencies; however, the relationship is not directly due to a change in frequency. Rather, it arises from the geometry of the imaging process as noted in [13]. Developing the mathematical equations from the geometric perspective provides insight into the problem and sets the stage for analyzing the Omega-k algorithm from a signal processing point of view.

This chapter develops the SAR signal from the basic principles of radar and the SAR imaging geometry, and presents the most common frequency domain representation for the signal. Then, the frequency domain representation of the SAR signal is presented and discussed.

2.1 Basic Radar Processing

Understanding the basic principles of radar provides the necessary foundation for understanding synthetic aperture radar. At the most general level, a radar uses electromagnetic waves to detect targets and to determine the distance, or range, at which they are located. This is done by transmitting a known signal, often a chirp, and then listening for echos scattered by the targets. The angle to the target is inferred from the antenna pattern and the antenna pointing direction. Some radars transmit from one location and receive at another; however, the following development focuses on systems which receive the signal in the same location from which the signal is transmitted. In addition to range measurement, radars can also measure

echo power to obtain information about the target size and orientation and can infer velocities from Doppler frequencies. The radar signal and quadrature demodulation are addressed followed by a discussion on matched filtering.

2.1.1 Radar Signal

Prior to addressing the details of processing, the radar signal characteristics are explored in this section. Typically, the echos that are received are converted into complex-valued signals immediately after they are received, and it is important to understand both the echo and its complex counterpart.

Radars typically transmit a signal of the form [14]

$$y_1(t) = w(t)cos(2\pi f_0 t + \theta(t)), \tag{2.1}$$

where $w(t)$ is a window function, f_0 is the carrier frequency, and $\theta(t)$ is a phase function which defines the transmit modulation. Assuming a target is present, the transmitted signal travels out to the target, and some of the energy is scattered back towards the radar in the form of an echo. This echo travels back to the radar and is received after a time delay

$$\tau = \frac{2r}{c}, \tag{2.2}$$

where r is the range to the target. The received echo has a much smaller amplitude due to free-space propagation loss and the target's scattering properties. In addition, the target introduces a phase term. The received signal is

$$y_2(t) = A_{target} w(t-\tau) \cos[2\pi f_0 (t-\tau) + \theta(t-\tau) + \phi_{target}], \tag{2.3}$$

where A_{target} includes all of the scaling terms, and ϕ_{target} is the phase term introduced by the target. The signal in Equation (2.3) is turned into a complex valued signal by an operation known as quadrature demodulation. This technique is the same as I/Q demodulation used in digital communications with one additional step (see Appendix

B). The resulting signal is

$$v(t) = A_{target} w(t-\tau) e^{j\theta(t-\tau)} e^{-j2\pi f_0 \tau} e^{j\phi_{target}}. \tag{2.4}$$

The first two terms in (Equation (2.4)) are the delayed chirp, the second is a phase term determined by the echo delay and the radar carrier frequency, and the last is the phase term introduced by the target.

The goal of radar processing is to detect targets and to determine the range or distance at which they appear. In most radar applications, thermal noise introduced by the antenna and the receiver obscures the faint echos returned by the targets. This is generally modeled as additive white Gaussian noise, and the received signal is

$$v(t) = A_{target} w(t-\tau) e^{j\theta(t-\tau)} e^{-j2\pi f_0 \tau} e^{j\phi_{target}} + \eta(t), \tag{2.5}$$

where $\eta(t)$ is the white noise process. To maximize the probability of detection, it is desirable to maximize the peak signal to noise ratio (SNR). The filter which performs this function is referred to as the matched filter and is discussed in the next section.

2.1.2 Matched Filter

The matched filter is optimal in the sense that it maximizes the SNR for a given signal of interest. While maximizing the SNR makes it easier to detect targets, it is also important to determine the range at which they appear, and the filter must place the peak of the resulting signal in the position which corresponds the range at which the target is located. Finally, the filter must localize the energy around that point so that targets which are close together can be distinguished.

Understanding the development of the matched filter is necessary for the analysis of the Omega-k algorithm in Chapter 4. The following development comes from [14], with minor changes to the variable names. The signal to noise ratio at time ν is expressed as

$$SNR = \frac{\left| \frac{1}{2\pi} \int_{-\infty}^{\infty} V(\Omega) H(\Omega) e^{j\Omega\nu} d\Omega \right|^2}{\frac{N_0}{4\pi} \int_{-\infty}^{\infty} |H(\Omega)|^2 d\Omega}, \tag{2.6}$$

Table 2.1: Time domain operations and their frequency domain equivalents. These properties are found in most introductory texts on signal processing, a good reference is [15].

Time Domain Operation	Time Domain	Frequency Domain
Time Reversal	$x_2(t) = x_1(-t)$	$X_2(jw) = X_1^*(-jw)$
Complex Conjugation	$x_2(t) = x_1^*(t)$	$X_2(jw) = X_2(-jw)$
Time Delay	$x_2(t) = x_1(t-\tau)$	$X_2(jw) = e^{-jw\tau}X_2(jw)$
Convolution	$x_3(t) = x_1(t) * x_2(t)$	$X_3(jw) = X_1(jw)X_2(jw)$

where $H(\Omega)$ is the frequency response of the applied filter, and $V(\Omega)$ is the Fourier transform of the received signal $v(t)$. The numerator in Equation (2.6) is the instantaneous power of the desired signal at the point ν, and the denominator is the output noise power when white noise with a power spectral density $N_0/2$ Watts/Hertz is assumed. Applying the Schwarz inequality to the integral in the numerator yields [14]

$$SNR \leq \frac{\frac{1}{2\pi}\int_{-\infty}^{\infty}|V(\Omega)e^{j\Omega\nu}|^2 d\Omega \int_{-\infty}^{\infty}|H(\Omega)|^2 d\Omega}{\frac{N_0}{4\pi}\int_{-\infty}^{\infty}|H(\Omega)|^2 d\Omega}, \tag{2.7}$$

where equality is achieved if and only if [14]

$$H(\Omega) = \alpha[V(\Omega)e^{j\Omega\nu}]^*, \tag{2.8}$$

where α is an arbitrary constant, and ν is the time where the SNR is maximized. The magnitude of α does not affect the SNR ratio because it appears in both the numerator and the denominator in Equation (2.7). Equation (2.8) is the frequency response of the filter which maximizes the peak SNR.

The second requirement established for the filter is to place the point where the SNR is maximized at the time corresponding to the range of the target. As noted in the previous section, the signal delay, τ, is directly related to the range at which the target appears and should, therefore, be the location where the SNR is maximized.

The equation for this filter is

$$H(\Omega) = \alpha[V(\Omega)e^{j\Omega\tau}]^*. \tag{2.9}$$

Next, the time domain representation for the filter is determined from the properties listed in Table 2.1. The phase ramp in Equation (2.9) corresponds to a time advancement by τ, and the complex conjugation corresponds to both time reversal and complex conjugation in the time domain. Applying those changes to the quadrature demodulated radar signal in Equation (2.4) yields

$$h(t) = \alpha w^*(-t)e^{-j\theta(-t)}e^{j2\pi f_0\tau}e^{-j\phi_{target}} \tag{2.10}$$

as the impulse response of the filter. The only problem with this expression is that it depends on both the range to the target and the phase term introduced by the target; neither of which are known *a priori*. However, since α can be any arbitrary constant, choosing it to include the complex conjugate of these terms,

$$\alpha = \alpha_{new}e^{-j2\pi f_0\tau}e^{j\phi_{target}}, \tag{2.11}$$

yields a target independent filter

$$h(t) = \alpha_{new}w(-t)e^{-j\theta(-t)}, \tag{2.12}$$

where α_{new} is an arbitrary constant and the filter is merely the time-reversed, complex-conjugate of the complex valued radar chirp, undelayed in time. As noted previously, the radar actually transmits a real signal. However, applying quadrature demodulation to the transmitted chirp in Equation (2.1) yields

$$h(t) = w(t)e^{j\theta(t)} \tag{2.13}$$

as the corresponding complex signal. It is very significant that the time origin of Equation (2.13) and the time origin of Equation (2.12) are matched. The window

function $w(t)$ could be centered at $t = 0$, begin at $t = 0$, or end at $t = 0$. Whatever the choice, the same window function must be used to generate the filter so that the target is properly placed along the time axis.

The last thing the filter must do is strongly localize the energy of the pulse around the time corresponding to the range of the target. The means for satisfying this requirement are not clearly evident until the output of the filter is considered in the frequency domain. Let $c(t)$ denote the complex radar chirp

$$c(t) = w(t)e^{\theta(t)}, \tag{2.14}$$

and let $C(\Omega)$ denote the Fourier transform of that chirp. If we assume that the received echo was amplified such that the magnitude of the echo is equal to the magnitude of $c(t)$, the Fourier transform of the echo is

$$V(\Omega) = C(\Omega)e^{-j\Omega\tau}e^{-j2\pi f_0\tau}e^{j\phi_{target}}, \tag{2.15}$$

and the Fourier transform of the filter is

$$H(\Omega) = \alpha_{new}C^*(\Omega). \tag{2.16}$$

Performing the filtering in the frequency domain yields

$$\begin{aligned} H(\Omega)V(\Omega) &= \alpha_{new}C^*(\Omega)C(\Omega)e^{-j\Omega\tau}e^{-j2\pi f_0\tau}e^{j\phi_{target}} \\ &= \alpha_{new}|C(\Omega)|^2e^{-j\Omega\tau}e^{-j2\pi f_0\tau}e^{j\phi_{target}}. \end{aligned} \tag{2.17}$$

The only aspect of the matched filter which can be modified is the scale term α_{new}. Unfortunately, multiplying by a scalar only alters the amplitude and phase of the complex signal in the time domain. It does not affect in any way the localization of energy.

Of the terms in Equation (2.17), the first exponential is merely a time delay, and the other exponential terms merely change the phase of the signal. The only term

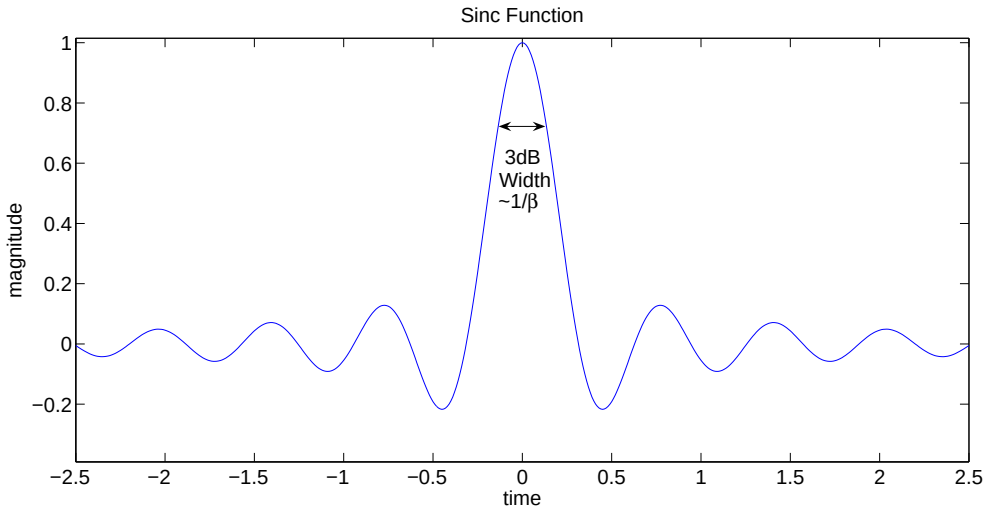

Figure 2.1: The plot of a sinc function. Much of the energy of a sinc function is located around the peak of the function. The width of the main lobe is often characterized by the 3dB width which is inversely proportional to the bandwidth β of the signal.

which affects the shape of the signal envelope in the time domain is $|C(\Omega)|^2$ – the task becomes properly choosing that term. A simple choice is $\text{rect}(\Omega/\beta)$ which corresponds to a sinc function of width $1/\beta$ in the time domain. This is shown in Figure 2.1. A common metric for the localization of energy is the 3dB width of the time domain signal indicated in the same figure. The 3dB width is commonly accepted as the resolution of the system, i.e. the minimum distance targets must be separated to be individually resolved. For the sinc function, this distance is approximately equal to $1/\beta$, where β is the bandwidth[1].

In practice, a rect is not achieved in the frequency domain; however, linear FM chirps with high time-bandwidth products come very close. Other choices for $|C(\Omega)|^2$ can be devised; the important criteria is that the energy of the corresponding time domain signal is strongly localized around the origin.

There are a couple aspects of matched filtering which deserve further comment. First, under the assumptions used to develop Equation (2.12), the peak amplitude of the signal output by the matched filter is the energy of the echo. This is seen by

[1]The bandwidth is the entire width of the signal's support in the frequency domain.

calculating the inverse Fourier transform of Equation (2.12) at $t = \tau$:

$$\begin{aligned}
\tilde{v}(\tau) &= \int_{-\infty}^{\infty} H(\Omega)V(\Omega)e^{j\Omega\tau}d\Omega \\
&= \int_{-\infty}^{\infty} \alpha_{new}|C(\Omega)|^2 e^{-j\Omega\tau}e^{-j2\pi f_0\tau}e^{j\phi_{target}}e^{j\Omega\tau}d\Omega \\
&= \int_{-\infty}^{\infty} \alpha_{new}|C(\Omega)|^2 e^{-j2\pi f_0\tau}e^{j\phi_{target}}d\Omega \\
&= \alpha_{new}e^{-j2\pi f_0\tau}e^{j\phi_{target}}\int_{-\infty}^{\infty} |C(\Omega)|^2 d\Omega \\
&= \alpha_{new}e^{-j2\pi f_0\tau}e^{j\phi_{target}}\int_{-\infty}^{\infty} |c(t)|^2 dt \qquad (2.18) \\
&= \alpha_{new}e^{-j2\pi f_0\tau}e^{j\phi_{target}}E_c, \qquad (2.19)
\end{aligned}$$

where E_c is the energy of the received chirp, and the second to last step requires Parseval's theorem. The magnitude of Equation (2.19) is the energy of the received echo scaled by the magnitude of α_{new}. As previously noted, the magnitude of α_{new} does not affect the resulting SNR. The matched filter achieves the optimal SNR by reducing all of the frequency domain phase modulation to linear phase ramps and squaring the magnitude of the frequency domain signal. This observation is revisited in Chapter 4 when the Omega-k algorithm is analyzed.

The second observation is that the phase of Equation (2.18) is entirely determined by the distance to the target and the complex phase term introduced by the target. In interferometric systems, two spatially separated antennas are used to receive echos from the target. When the range between one antenna and the target differs from the range between the other antenna and the target, that phase term differs by an amount proportional to the difference between the two ranges, and the angle to the target can determined rather precisely. The one caveat is that Equation (2.18) is usually sampled, and in general, the target samples for the two signals do not exactly correspond. However, when $|C(\Omega)|^2$ is symmetric, $|C(\Omega)|^2 e^{-j\Omega\tau}$ is conjugate-symmetric and the corresponding time domain signal is real. Thus, the phase of the entire time domain signal is determined by the distance to the target and the complex

phase term introduced by the target. Even when the samples are slightly misaligned, the appropriate phase term is obtained.

Summarizing, the matched filter maximizes the SNR of the processed target echo at the location corresponding to its range, and the transmitted chirp determines how localized the energy is around that point. The result of the filtering process is

$$\tilde{v}(t) = \alpha_{new} h(t-\tau) e^{-j2\pi f_0 \tau} e^{j\phi_{target}}, \tag{2.20}$$

where $h(t-\tau)$ is the inverse Fourier transform of $|C(w)|^2 e^{-j\Omega\tau}$, and the radar system detects targets by identifying peaks in the received signal; the range is determined from the time delay associated with the peak. Before proceeding, Equation (2.20) is changed from an equation in time to an equation in range by a change of variables according to Equation (2.2). After that change of variables, the signal in Equation (2.20) becomes

$$V(\rho) = h\left(\frac{2}{c}(\rho - R)\right) e^{-j2\pi f_0 \frac{2}{c} R} e^{j\phi_{target}}, \tag{2.21}$$

where ρ is the independent position in range. To complete the transition to spatial quantities, the radar carrier frequency is converted to cycles per meter according to $f_{\rho 0} = 2f_0/c$ to yield

$$V(\rho) = h\left(\frac{2}{c}(\rho - R)\right) e^{-j2\pi f_{\rho 0} R} e^{j\phi_{target}}, \tag{2.22}$$

and substituting a new function $h_\rho(r) = h(2r/c)$ into Equation (2.22) yields the final result

$$V(\rho) = h_\rho(\rho - R) e^{-j2\pi f_{\rho 0} R} e^{j\phi_{target}}. \tag{2.23}$$

As noted previously, the first exponential term in Equation (2.23) is important for interferometric systems. It is also important for SAR systems, as addressed in the next section.

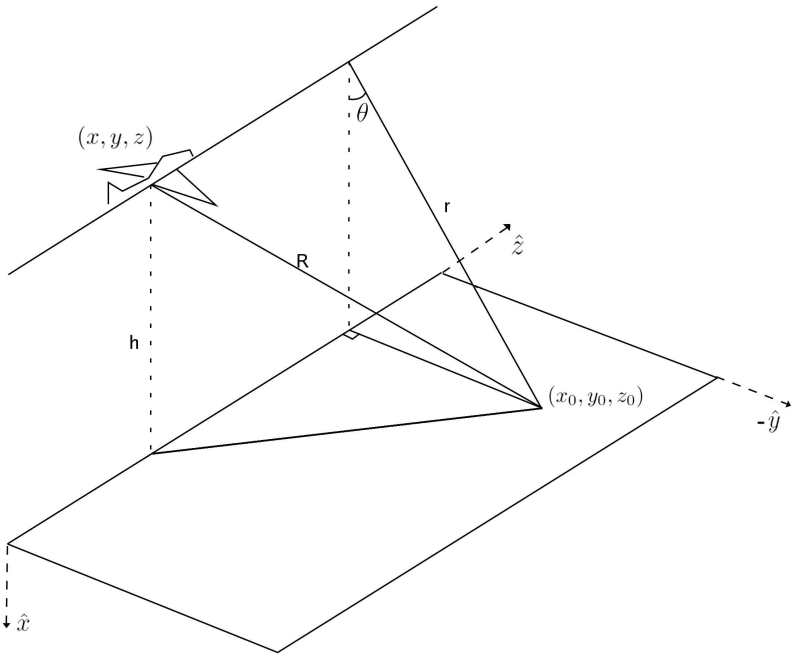

Figure 2.2: An illustration of the three dimensional geometry for stripmap SAR sensors. The slant range of closest approach is denoted r. Adapted from [16].

2.2 Time Domain SAR Signal

Unlike surveillance radar systems such as those used in air traffic control, SAR systems are not operated from a single location. Instead, they are moved along a deterministic trajectory to intentionally vary the distance between the radar and the stationary targets. As noted in the previous section, the first exponential term in Equation (2.23) is a phase term which depends on the range to the target. By moving the SAR system along the predefined trajectory, that phase changes in a deterministic way and provides the means for achieving a high azimuth resolution.

The most common way to vary the location of the SAR sensor is along a linear trajectory as illustrated in Figure 2.2, where the aircraft represents the SAR platform. The $\hat{z}$ direction along the linear trajectory is commonly referred to as the azimuth direction. In that figure, the target is located at (x_0, y_0, z_0), and r is the minimum distance between the target and the linear trajectory. This minimum distance, r, is important for SAR processing and is termed the slant range of closest approach

(SRCA). When the platform is at location z along the trajectory, the range to the target is

$$R = \sqrt{r^2 + (z - z_0)^2}. \tag{2.24}$$

Incorporating this expression for the range into Equation (2.23), the received signal for a target located at (r, z_0) is

$$V(\rho, z) = h_\rho \left(\rho - \sqrt{r^2 + (z - z_0)^2} \right) e^{-j2\pi f_{\rho 0} \sqrt{r^2 + (z - z_0)^2}} e^{j\phi_{target}}. \tag{2.25}$$

By transmitting the signal and receiving echos from many points along the linear trajectory, Equation (2.25) is effectively sampled in the azimuth direction. The collected data forms a 2-dimensional signal where range and azimuth are the two dimensions. An important observation is that the target response depends only on the target's azimuth location and its SRCA. Targets located in 3-dimensional space are projected onto 2 dimensions, SRCA and azimuth. A coordinate system consistent with that projection is a cylindrical coordinate system with the z axis aligned along that linear trajectory, r corresponding to the SRCA, and θ as the angle in the xy-plane. In this coordinate system, it is possible to address the antenna pattern.

As with traditional radar systems, the antenna pattern limits the spatial volume from which echos are received. A common configuration for SAR imaging is to point the antenna in a fixed direction with respect to the linear trajectory. This configuration is referred to as stripmap SAR. The angle at which the antenna is pointed determines the mode in which the SAR system is operated. When the antenna is pointed in a direction perpendicular to the linear trajectory, the SAR system is operating in the broadside mode. Otherwise, the SAR system is operating in squint mode. While the figures used in the following discussion portray a SAR system operating in broadside mode, the discussion is applicable for both.

As the platform progresses in the azimuth direction, targets enter and leave the antenna beam as shown in Figure 2.3 where only the SRCA and the azimuth position are represented. In general, the antenna beamwidth for a given target depends on the angle θ to the target, however, significant insight is obtained by assuming that

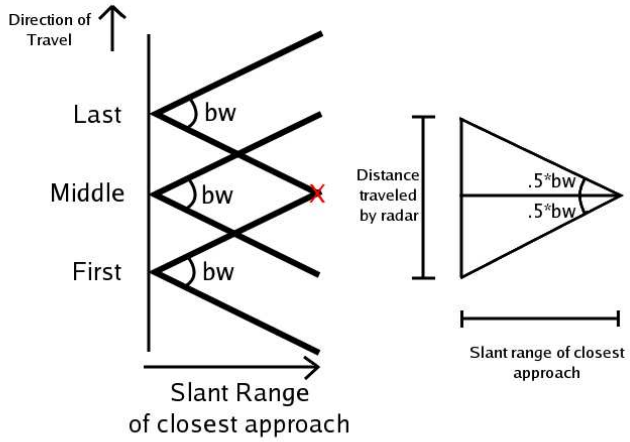

Figure 2.3: An illustration of the two dimensional geometry for stripmap SAR. On the left, a simplified radar antenna pattern is shown for three positions along the trajectory which correspond to the points where the target is illuminated by the leading edge of the antenna pattern, by the center of the antenna pattern, and by the trailing edge of the antenna pattern. The target is shown as a red X, and the antenna beamwidth is denoted by bw. The distance traveled by the radar is shown on the right.

the antenna pattern does not vary with θ. Under this assumption, the effect of the 2-way, antenna pattern can be represented by a window function

$$A\left(\frac{z-z_0}{r}\right). \tag{2.26}$$

Incorporating the antenna window function along with the other amplitude scaling terms into Equation (2.25), the full SAR signal is

$$\begin{aligned} V(\rho,z) &= \frac{k}{\left[(z-z_0)^2+r^2\right]^2} A\left(\frac{z-z_0}{r}\right) h_\rho\left(\rho-\sqrt{r^2+(z-z_0)^2}\right) \\ &\qquad e^{-j2\pi f_{\rho 0}\sqrt{r^2+(z-z_0)^2}} e^{j\phi_{target}}, \end{aligned} \tag{2.27}$$

where k is a constant which includes the transmit power, the target's radar cross-section, the radar wavelength, and a factor of $1/(4\pi)^3$. The denominator of the first

term in Equation (2.27) is the range spreading loss. There are additional sources of attenuation such as atmospheric attenuation, but they are assumed to be negligible.

The last point to be noted is the length of the trajectory over which echos from a particular target are received. This development requires the introduction of a new angle

$$\phi = \tan^{-1}\left(\frac{z_0 - z}{r}\right), \tag{2.28}$$

which is referred to as the look angle in this thesis. For a target with a SRCA of r, echos are received over a segment in azimuth of length

$$\delta z = r[\tan(\phi_{max}) - tan(\phi_{min})], \tag{2.29}$$

where ϕ_{max} and ϕ_{min} are maximum and minimum look angles from which significant energy is received through the antenna. This expression reduces to

$$\delta z = 2r \tan\left(\frac{\theta_b}{2}\right) \tag{2.30}$$

for broadside mode SAR, where θ_b is the antenna beamwidth. For an antenna with a beamwidth exceeding 54 degrees, pointed broadside, the length in the azimuth direction can exceed the target's SRCA which can be multiple kilometers. This effect is analyzed further in Section 3.2.

2.3 Frequency Domain Representation

From the time domain expression for the received signal in Equation (2.27), we can compute the Fourier transform of the signal. While a closed form solution to the Fourier transform of Equation (2.27) is not known, an approximate version is typically developed using the principle of stationary phase (POSP) approximation which is discussed in Chapter 6. In this section, the Fourier transform in range is presented followed by the result of the azimuth Fourier transform. Then, the resulting frequency domain SAR signal is analyzed.

The range Fourier transform depends only on the chosen radar chirp. The only term in Equation (2.27) which depends on ρ is h_ρ. Assuming that an ideal matched filter was applied, the Fourier transform of h_ρ is entirely real, and the range Fourier transform of Equation (2.27) is

$$\begin{aligned} V(f_\rho, z) &= \frac{k}{\left[(z-z_0)^2 + r^2\right]^2} A\left(\frac{z-z_0}{r}\right) H_\rho(f_\rho) e^{-j2\pi f_\rho \sqrt{r^2+(z-z_0)^2}} \\ &\quad e^{-j2\pi f_{\rho 0}\sqrt{r^2+(z-z_0)^2}} e^{j\phi_{target}}, \end{aligned} \tag{2.31}$$

where $H_\rho(f_\rho)$ is the Fourier transform of $h_\rho(\rho)$ and the first exponential is the delay term. Combining the first two exponential terms yields

$$\begin{aligned} V(f_\rho, z) &= \frac{k}{\left[(z-z_0)^2 + r^2\right]^2} A\left(\frac{z-z_0}{r}\right) H_\rho(f_\rho) \\ &\quad e^{-j2\pi (f_\rho + f_{\rho 0})\sqrt{r^2+(z-z_0)^2}} e^{j\phi_{target}}. \end{aligned} \tag{2.32}$$

Evaluating the azimuth Fourier transform of Equation (2.32) is complicated by the square-root term in the exponential and the antenna weighting function. The standard approach for obtaining a closed-form solution involves invoking the principle of stationary phase approximation. The full derivation of this step, including all of the necessary simplifications, is provided in Appendix A. From Equation (A.18), the result is

$$\begin{aligned} V(f_\rho, f_z) &= k\frac{((f_\rho + f_{\rho 0})^2 - f_z^2)^{\frac{5}{4}}}{r^{\frac{7}{4}}(f_\rho + f_{\rho 0})^3} A\left(\frac{f_z}{\sqrt{(f_\rho + f_{\rho 0})^2 - f_z^2}}\right) H_\rho(f_\rho) \\ &\quad e^{-j\frac{\pi}{4}} e^{j\phi_{target}} e^{-j2\pi r\sqrt{(f_\rho+f_{\rho 0})^2 - f_z^2} - j2\pi f_z z_0}. \end{aligned} \tag{2.33}$$

The frequency domain support of the SAR signal is entirely determined by the $H_\rho(f_\rho)$ and the weighting function of the antenna. $H_\rho(f_\rho)$ is only a function of range frequency, and limits the support of the function in that dimension. The antenna weighting function limits the azimuth frequencies, however the limitation depends on the range frequency. This relationship is best understood after the relationship between the look angle ϕ and azimuth frequency is developed.

The antenna weighting function operates on the ratio

$$\frac{z_0 - z}{r} = \tan(\phi), \tag{2.34}$$

where ϕ is the look angle. Because the same weighting function is used in both the time and the frequency domains, there is a direct relationship between the look angle ϕ and the azimuth frequency. Equating the argument to the weighting function in Equation (2.33) to $\tan(\phi)$, we have

$$\frac{f_z}{\sqrt{(f_\rho + f_{\rho 0})^2 - f_z^2}} = \tan(\phi). \tag{2.35}$$

The left side of Equation (2.35) approaches infinity as

$$f_z \rightarrow (f_\rho + f_{\rho 0}), \tag{2.36}$$

so that $(f_\rho + f_{\rho 0})$ represents the maximum azimuth frequency that is possible with an isotropic antenna. For more realistic antenna patterns, further insight is obtained by solving for f_z to yield

$$\begin{aligned} f_z &= \pm(f_\rho + f_{\rho 0}) \frac{\tan(\phi)}{\sqrt{1 + \tan^2(\phi)}} \\ &= \pm(f_\rho + f_{\rho 0}) \sin(\phi) \\ &= (f_\rho + f_{\rho 0}) \sin(\phi), \end{aligned} \tag{2.37}$$

where the sign ambiguity is resolved by noting that in Equation (2.35) the sign of f_z must be the same as the sign of $\tan(\phi)$ which has the same sign as $\sin(\phi)$ between -90 and 90 degrees.

With a relationship between the look angle and the azimuth frequency, the frequency domain support of the SAR signal is presented. Using the angle at which the antenna pattern drops to 3dB of its peak value, the corresponding azimuth frequency is given by Equation (2.37). Using that as the edge of the limit in the azimuth frequency direction, the frequency domain support for a SAR system operating in

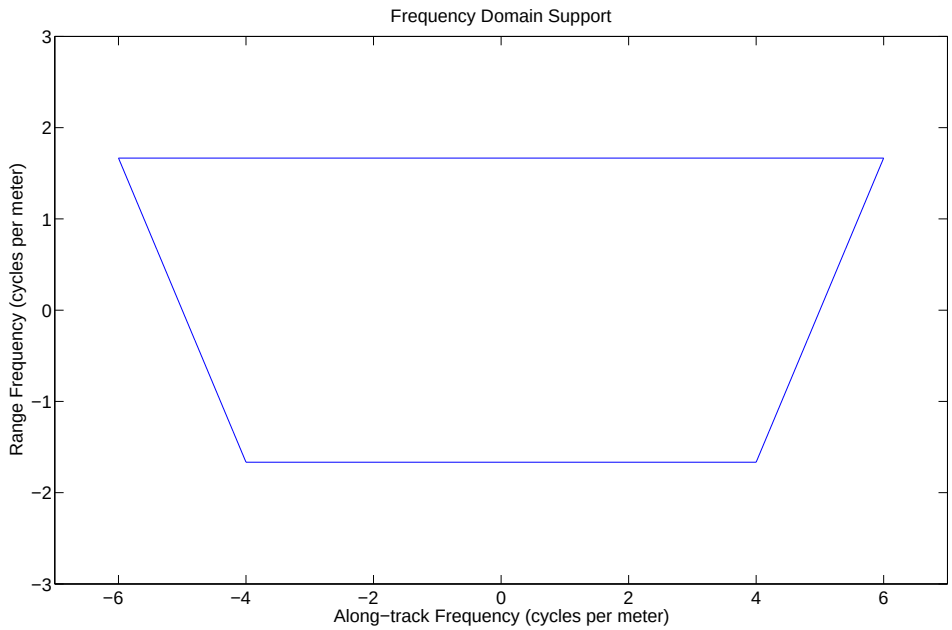

Figure 2.4: A plot of the frequency domain support of the SAR signal for an L-band SAR with a 250 MHz range chirp and a 60 degree azimuth beamwidth. The frequency axes are spatial frequencies.

broadside mode is shown in Figure 2.4. It is interesting to note that the frequency domain support of the signal is not symmetric through the origin. In Chapter 4, it is shown that this asymmetry is aggravated when the signal is processed using the Omega-k algorithm. The implications of this asymmetry are addressed in that chapter.

Chapter 3

SAR Data Collection

In the previous chapter, the equation for the SAR signal is developed. In this chapter, the conditions under which data can be properly processed are addressed. One important design parameter is the length of so-called "fast-time" that the receiver records the echos from each pulse. This length of time is referred to as the range gate and affects the amount of data that must be recorded and the size of the usable image that is produced. In the azimuth or "slow-time" direction, it is often necessary to segment the data prior to processing. The size of the segments also affects the usable portion of the processed image. In this chapter, these two ideas are addressed.

3.1 Range Gate

The two important aspects of the range gate are the time of the first sample and the time of the last sample. To reduce the data storage requirements, data is not collected until a target return is expected. For airborne platforms, the first target return is expected for a range equal to the height that the aircraft flies above the imaged area. As this is a known distance, a receive delay is built into the system so that the first sample is taken just before this first echo is expected to arrive. This delay is referenced to the time that the beginning of the chirp is transmitted and is calculated according to

$$T_d = 2\frac{r_{ca,min}}{c}, \tag{3.1}$$

where $r_{ca,min}$ is the minimum distance at which targets are expected to appear.

The second aspect concerns the length of the range gate. The range gate directly determines extent of the final image in the range direction; however, the signal from Equation (2.27) is only collected for a fraction of the SRCA positions

represented in the processed image. For each pulse that is transmitted, the range to the last target for which the entire echo is collected is

$$R_{last} = \frac{c}{2}(T_d + T_{rg} - T_p), \tag{3.2}$$

where T_d is the receive delay, T_{rg} is the range gate, and T_p is the chirp length. In Figure 3.1(a), the associated distances are labeled on the bar above the antenna pattern. On the edge of the antenna pattern, a target which appears at that range has a SRCA which is calculated according to

$$r_{ca,max} = \frac{c}{2}(T_d + T_{rg} - T_p)\cos\left(\frac{\theta_b}{2}\right), \tag{3.3}$$

where θ_b is the antenna beamwidth. The entire echo for all targets with a SRCA between $r_{ca,min}$ and $r_{ca,max}$ is collected whenever the target is located in the antenna beamwidth–$r_{ca,min}$ and $r_{ca,max}$ define the limits of the usable portion of the image which is bounded by the red, vertical, dashed lines in Figure 3.1. Any targets outside of that area cannot be properly processed because the full signal is not recorded. It is important to note that the distance between the red lines is reduced as the beamwidth increases, or the antenna is pointed forward. The important quantity is the maximum angle at which targets are illuminated by significant energy.

When the antenna beamwidth is relatively narrow, the effect just discussed is not very significant. However, for wide-beamwidth SAR systems, the effect introduces an additional trade-off to be considered in the design process. According to Equation (3.3), the maximum range can be extended by increasing the range gate or decreasing the pulse length. The trade-off with increasing the range gate is that more data must be stored. While the pulse length does not directly affect the range resolution, there is a minimum length for a given chirp bandwidth for which the pulse length does not significantly affect the resolution. The chirp length also directly affects the final SNR. As these are all important considerations, quantifying the effect of the design parameters on the size of the usable swath width is necessary for making appropriate design choices.

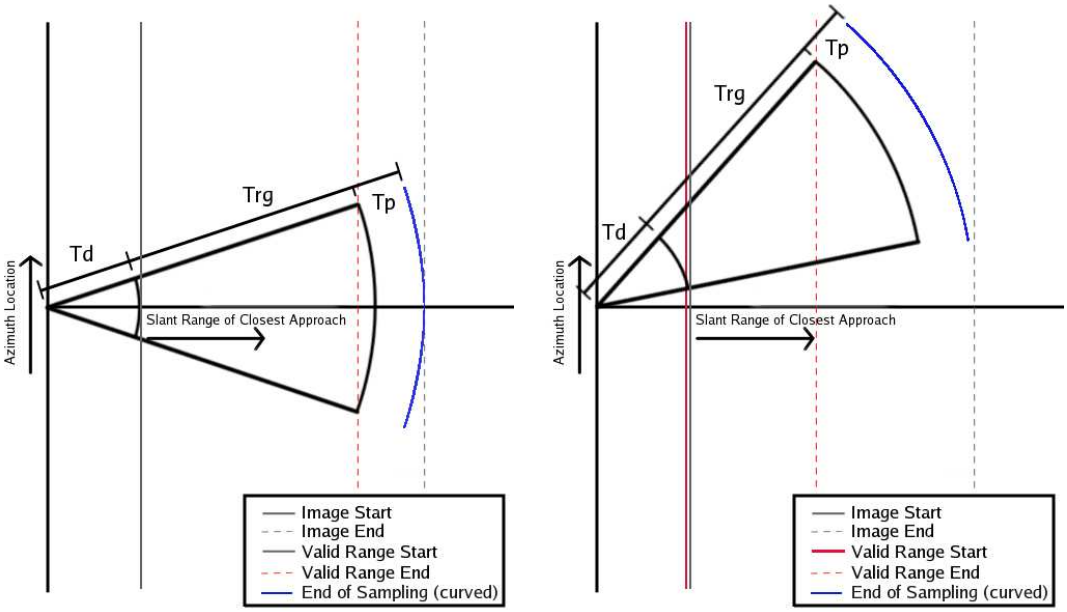

(a) Broadside (b) Squinted

Figure 3.1: An illustration of the limits on the valid SRCAs imposed by the antenna pattern, the receive delay (Td), the range gate (Trg), and the pulse length (Tp). A full resolution image can be made only over the ranges between the red dashed lines.

The effect of choosing a particular range gate and a particular pulse length is analyzed for a few cases relevant to the work being done in our research group. In Figure 3.2, plots are provided which illustrate the direct relationship between the antenna beamwidth and the maximum slant range swath width for four pulse lengths and two range gates. The slant range swath width is the difference between the maximum SRCA and the minimum SRCA. It is calculated according to

$$\begin{aligned} W_{sl} &= \frac{c}{2}(T_d + T_{rg} - T_p)\cos(\phi_{max}) - \frac{c}{2}T_d \\ &= \frac{c}{2}T_{rg}\cos(\phi_{max}) - \frac{c}{2}T_p\cos(\phi_{max}) - \frac{c}{2}T_d(1 - \cos(\phi_{max})). \end{aligned} \tag{3.4}$$

For our work at BYU, a beamwidth of 60 degrees is desirable and we are currently using a 1μs pulse. If we limit the range gate to 4096 samples (top plot in Figure 3.2), the slant range swath width is about 750m, a little over half the distance represented

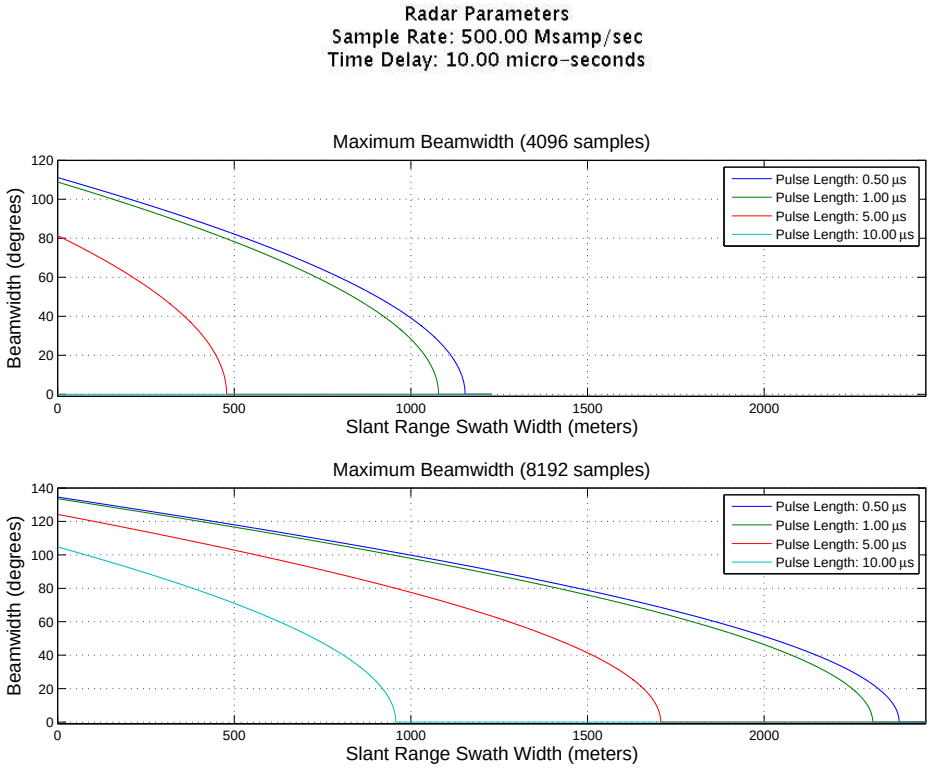

Figure 3.2: Plots of the combined effect of the antenna beamwidth, the time delay, the range gate, and the pulse length on the usable swath width. The range gate for the bottom plot is twice that of the top plot.

by the range samples. When the range gate is doubled, the slant range swath width increases to 1750m which is about 70 percent of the distance represented by the range samples. This is a significant increase both in the usable swath width and in the fraction of the resulting image which is usable.

The effect of the pulse length is also significant. It is clear from the plots that choosing a pulse length which is a significant fraction of the range gate has a limiting effect on the slant range swath width. While cutting the pulse length in half does not double the slant range swath width, using the minimum pulse length which does not significantly degrade the resulting range resolution or achieved SNR can significantly increase the slant range swath width.

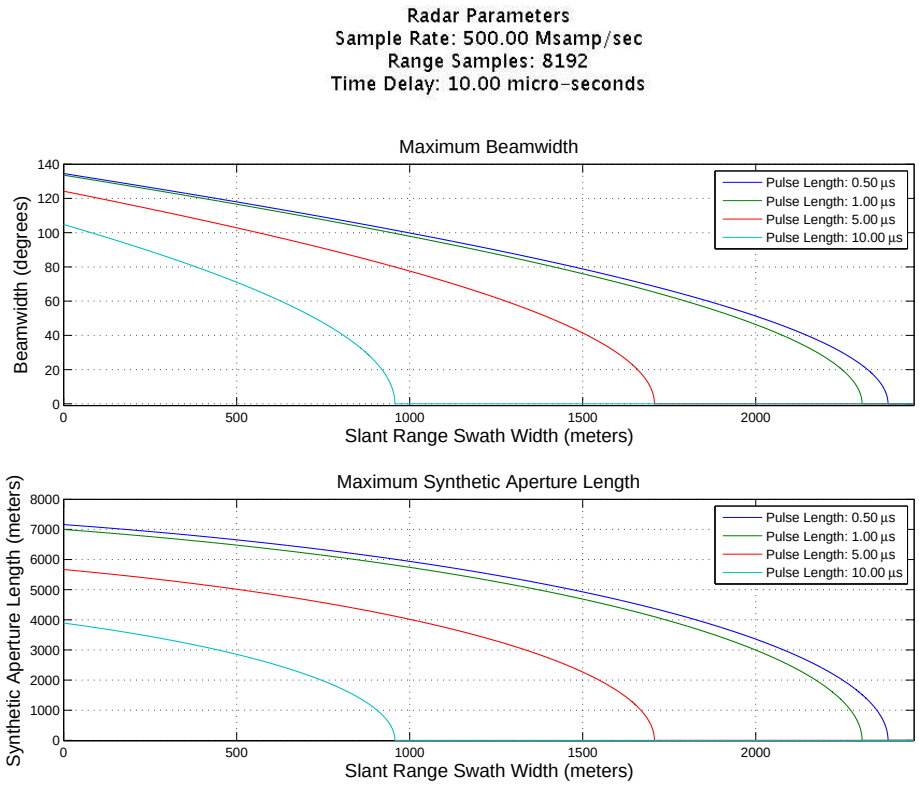

Figure 3.3: Plots of the synthetic aperture length corresponding to the radar parameters in Figure 3.2 for 8192 range samples. The top plot shows the maximum beamwidth for a given slant range swath width, and the bottom plot shows the synthetic aperture length for a given swath width assuming the maximum beamwidth is used.

3.2 Segment Processing

The previous section addressed the collection of data in the range direction. In the azimuth direction, data can be collected as long as there is space to store it. However, processing large amounts of data requires large amounts of memory and it becomes necessary segment the data in the azimuth direction during processing. This section addresses both the minimum segment size and the process for identifying the properly compressed pixels in larger processed segments. These ideas are first developed for the simplified antenna pattern from Chapter 2, and then for realistic antenna patterns.

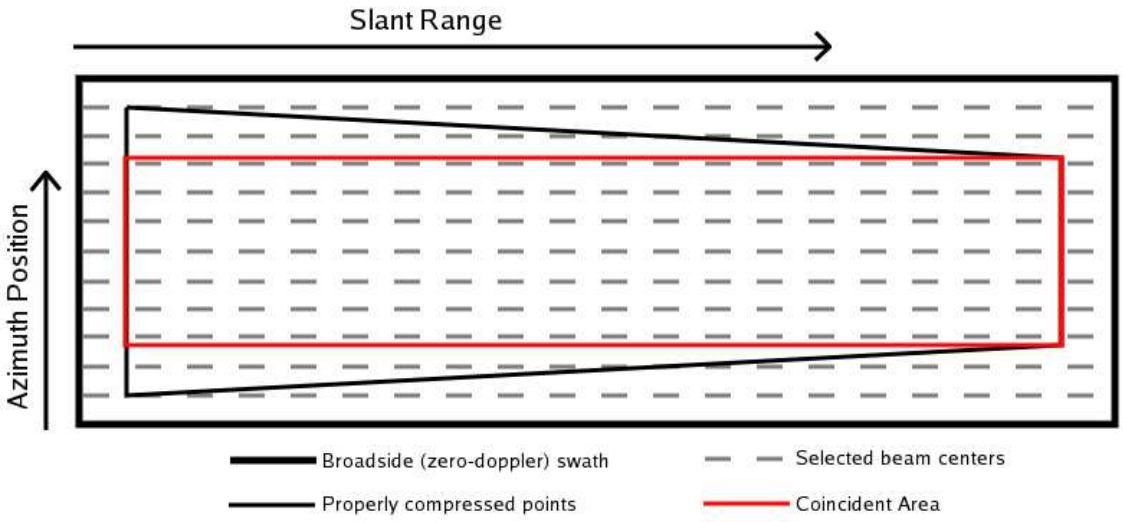

Figure 3.4: An illustration of the collected data for a SAR system operating in broadside mode.

3.2.1 Simple Antenna Pattern

In Section 2.2, it is noted that the response from a target for a broadside SAR system covers an azimuth distance

$$\delta z = 2r \tan\left(\frac{\theta_b}{2}\right), \tag{3.5}$$

where r is the SRCA, and θ_b is the antenna beamwidth seen by all targets. In calculating the maximum azimuth distance, one could use slant range corresponding to the last sample of the range gate; however, all of the echos for targets located at this SRCA cannot be recorded because the range gate is too short. Instead, $r_{ca,max}$ from Equation (3.3) is used, and the resulting azimuth distance represents the minimum segment size which contains the entire signal for the target located in the center of the azimuth segment at $r_{ca,max}$. For every additional meter added to the segment size, the segment contains the entire signal for an additional meter worth of azimuth positions in the center of the segment. For this reason, the maximum azimuth length represents a sort of initial cost for processing the SAR signal.

Once the data in a segment is processed, it is desireable to retain only the portion which represents targets for which the entire signal is contained in the segment– these targets have been properly focused. When the data is processed using the Omega-k algorithm discussed in Chapter 4, they end up in the position corresponding to their SRCA in range and their zero-Doppler position in azimuth. Assuming the SAR system is operating in broadside mode, it is easy to identify the properly processed pixels. When the first pulse of the segment is sent out, the target located in an azimuth position one half of Equation (3.5) ahead of the platform is just entering the antenna beam. When the last pulse of the segment is sent out, the target located in an azimuth position one half of Equation (3.5) before the platform is just leaving the antenna beam. Therefore, the signal for all targets with a SRCA between $r_{ca,min}$ and $r_{ca,max}$ which appear between those two azimuth positions is entirely contained within the segment. This area is shown in Figure 3.4.

Ultimately, a continuous swath of properly processed data is desired. The easiest approach to achieving this result is to extract the pixels contained in the red box in Figure 3.4 and delay the next segment by the width of the red box. The drawback is that many near range pixels are properly processed more than once. For SAR systems with long range gates, it may be advantageous to segment the data in range for processing; however, doing so does increase the complexity of data handling and storage.

Extending the analysis to squint-mode SAR introduces an additional consideration. In the following, it is assumed that the range of angles over which the targets are viewed is constant for all targets. With the antenna squinted backwards, the radar pulses traverse the zero-Doppler swath at an angle as shown in Figure 3.5. Rather than appearing a distance from the edge of the zero-Doppler swath, the properly processed pixels are located a distance from the center of the antenna beam for the first and last pulses in the segment. Some of the pixels which are properly processed correspond to positions outside the zero-Doppler swath. These are outlined in a solid blue line in Figure 3.5. Because the Omega-k algorithm uses phase shifts in the frequency domain to place the targets, targets in these positions appear wrapped around

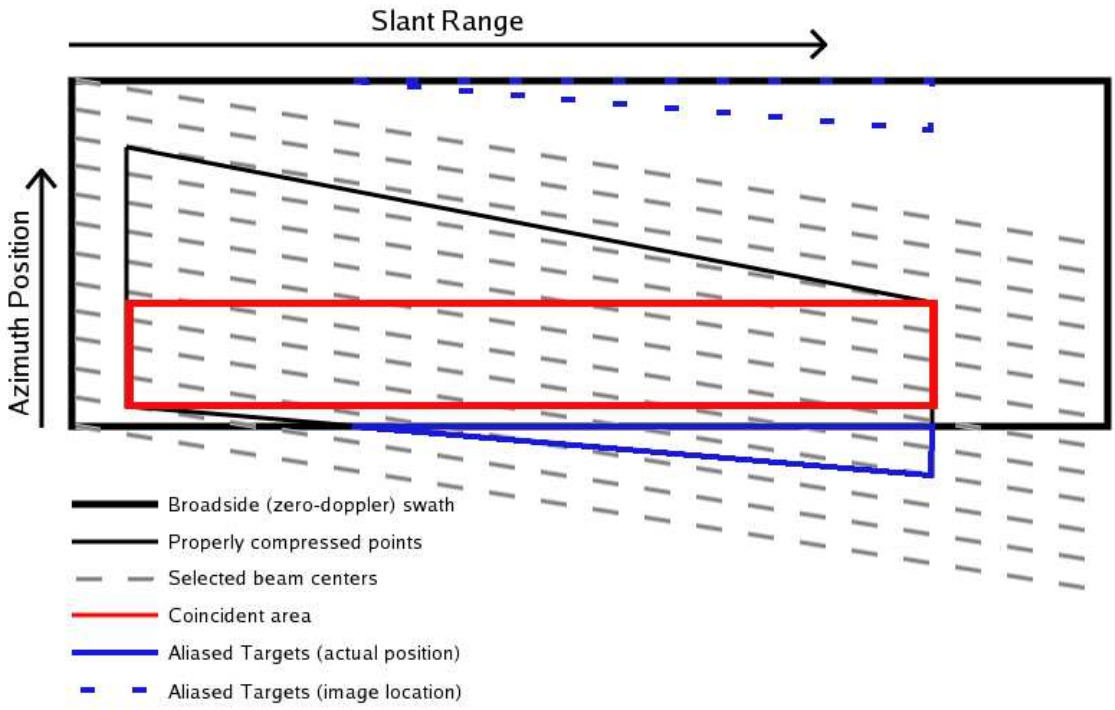

Figure 3.5: An illustration of the collected data for a SAR system operating in squint mode.

to the other side of the image and are enclosed by the dotted blue line in Figure 3.5. Once the positions of the pixels is determined, circular indexing properly identifies the desired azimuth samples.

For SAR systems operating in a significantly squinted configuration, it doesn't make sense to only retain the coincident pixels. The red box shown in Figure 3.1(b) eventually becomes empty. However, block processing is still possible if the same number of azimuth samples are taken at each SRCA. The only complication is associated with storing the data. A particularly simple approach is to store the data in its proper location with respect to the other data. While placing the data in the large array is somewhat difficult, retrieving the data for a given azimuth swath is very simple and can be fast when 2-d array is properly oriented.

3.2.2 Realistic Antenna Patterns

Realistic antenna patterns do not conform to the omni-directional assumption from Chapter 2. Extending the previous development to realistic antenna patterns is complicated by the fact that it is not generally possible to determine the precise angles θ in the xy-plane (see Figure 2.2) at which targets at a particular SRCA will appear. To overcome this challenge, the antenna pattern is rotated into a new coordinate system, and conservative limits are developed.

The first step in analyzing a more realistic antenna pattern is to transform it into a coordinate system consistent with the SAR imaging scenario. From Section 2.2, the desirable angles are θ in Figure 2.2 and ϕ in Equation (2.28). Once the antenna pattern is rotated into this coordinate system, the conservative limits are obtained by identifying the range of angles in θ at which significant energy could be received, and then searching over those angles for the maximum and minimum values of ϕ from which significant energy could be received[1].

With the maximum and minimum angles in ϕ identified, the valid positions for a SRCA r start at the position

$$z_{first} = z_{seg,start} + r\tan(\phi_{max}), \tag{3.6}$$

where $z_{seg,start}$ is the position of the SAR sensor at the beginning of the segment, and end at the position

$$z_{last} = z_{seg,end} + r\tan(\phi_{min}), \tag{3.7}$$

where $z_{seg,end}$ is the position of the SAR sensor at the end of the segment. Again, it is noted that when the valid positions fall outside the zero-Doppler swath for the segment, circular indexing identifies the processed targets.

[1]The amplitude of the antenna pattern at the maximum and minimum angle used in this calculation is important. The effect of a few choices on the focused point spread function is addressed in Chapter 6.

3.3 Conclusion

The usable portion of the processed image is an important consideration for the design of a SAR system. In range, the usable portion of the image is affected by the pulse length, the range gate, the receive delay, and the antenna beamwidth. In this chapter, the equations which relate those parameters to the usable swath width are developed and the plots showing how that width changes for various system configurations is presented. In the azimuth direction, there is a minimum segment size to process the data for a single azimuth position. The actual segment size is typically chosen to be much larger than the minimum size, and the equations for identifying the limits of the usable portion of the processed image in azimuth are presented.

Chapter 4

The Omega-k Algorithm

The Omega-k algorithm was originally proposed by Cafforio, Prati, and Rocca in [7], and has been presented in a number of papers and books in various forms (see [11] for a good list). In the original derivation, the mathematical equations were developed to describe the phenomenology and then reinterpreted into a new model referred to as the radiating reflector model. The processing steps were then justified by appealing to the characteristics of this new model. In [1], the development is more along the lines of signal processing, and the platform velocity is included to make time the independent variable in the azimuth direction. The development presented here is along the same lines as that in [1]. The main difference is the use of position as the independent variables in each dimension.

The challenge SAR processing poses is a non-separable, range-dependent point spread function. A range-dependent correlation filter could be used; however, the point spread function has a large region of support in the spatial domain and implementing such a filter requires an enormous amount of computation. The Omega-k algorithm presents an alternative approach to focusing the data which provides a result very similar to that of the matched filter.

In the following, the Omega-k algorithm is presented and analyzed. The first topic of the analysis is the SNR of the output. It is shown that with one modification, the Omega-k achieves nearly the same SNR as the matched filter. The second topic of the analysis, which is the main contribution of this chapter, is the effect of the Stolt mapping on the resulting point spread function. The influence of system design parameters is developed analytically, and then the effect of the Stolt mapping is explored through simulation.

4.1 Continuous Time Omega-k Algorithm

While the form varies between implementations, the Omega-k algorithm requires a change of variables in the frequency domain referred to as Stolt mapping, which is named after the man who originally proposed the method for use in imaging the geological structure of the earth [17]. This mapping reduces the phase variation in the frequency domain to phase ramps which center the signal around the azimuth position and SRCA of the target, a result very similar to that of the matched filter.

From the last term in Equation (2.33), the relevant portion[1] of the frequency domain phase is

$$\theta_{2dfft} = -2\pi r\sqrt{(f_\rho + f_{\rho 0})^2 - f_z^2} - 2\pi f_z z_0 \tag{4.1}$$

and consists of two terms. The last term in Equation (4.1) is precisely the linear ramp desired to center the signal on the azimuth position of the target. While the first term is a function of the target's SRCA, it is not a linear phase term and cannot be altered using phase multiplies because the SRCA r for the target is unknown. This term is changed into a linear phase ramp by a change of variables according to

$$\sqrt{(f_\rho + f_{\rho 0})^2 - f_z^2} = \tilde{f}_\rho + f_{\rho 0}, \tag{4.2}$$

which is the Stolt mapping. It is important to note that the mapping is 1-dimensional. The signal is mapped from frequencies f_ρ to $\tilde{f}_\rho$, and the mapping depends on the value of f_z. Performing the change of variables according to Equation (4.2) reduces the frequency domain phase to

$$\begin{aligned} \theta_{2dfft} &= -2\pi r(\tilde{f}_\rho + f_{\rho 0}) - 2\pi f_z z_0 \\ &= -\underbrace{2\pi \tilde{f}_\rho r}_{\text{SRCA Delay}} - \underbrace{2\pi f_z z_0}_{\text{Azimuth Delay}} - \underbrace{2\pi f_{\rho 0} r,}_{\text{Carrier Phase}} \end{aligned} \tag{4.3}$$

[1] There are additional phase terms in Equation (2.33), but they constant or associated with the antenna pattern. While the antenna pattern does cause phase variation in the frequency domain, it is not compensated by the Omega-k algorithm.

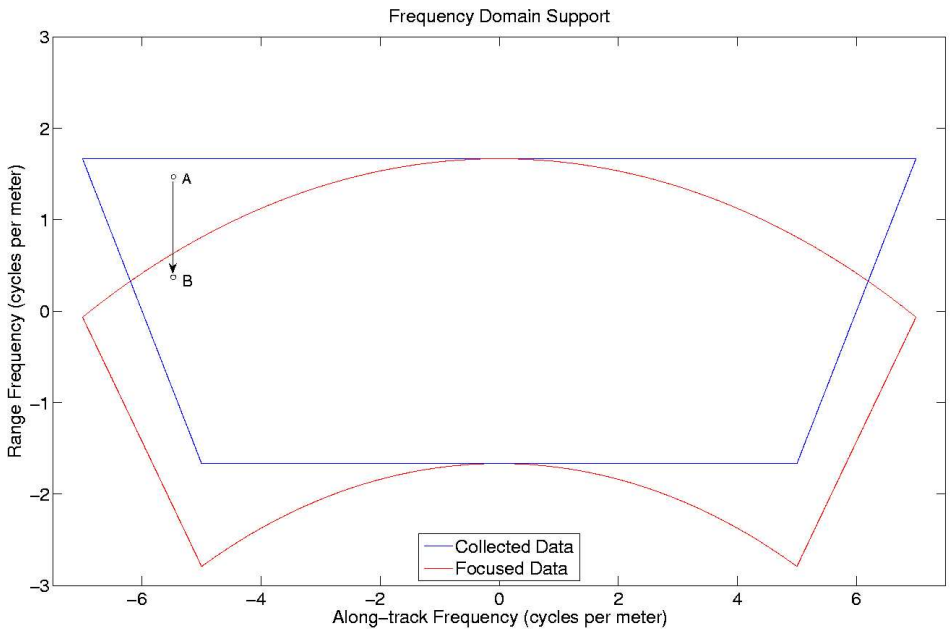

Figure 4.1: Plots of the frequency domain support of the SAR signal before (blue) and after (red) the Stolt mapping. The region of support is consistent with that of an L-band SAR system with a 60 degree beamwidth and a 500MHz range chirp. The effect of the Omega-k algorithm is to take energy from one place in the frequency domain and place it in a position where the phase is appropriate to focus the target (e.g. moving point A to point B).

where the first term is a shift in the range direction, the second is a shift in the azimuth direction, and the last is a constant phase term associated with the slant range of closest approach. This last term is desirable for interferometric SAR where two antennas are spatially separated and the difference in that phase term provides the information from which the 3-dimensional position of the detected scatterers is determined.

The Omega-k algorithm is an interesting approach to the problem of focusing the raw SAR data. The matched filter cannot be applied because the signal is range dependent. Instead, the Omega-k algorithm moves the frequency domain signal to a new position in the frequency domain where the phase is appropriate. This illustrated in Figure 4.1. The important relationship is that, even though the phase modulation in the frequency domain depends on the target's SRCA, the frequency domain map-

ping necessary to focus the data is the same regardless of the target's SRCA. The Omega-k algorithm exploits this relationship to focus the SAR data.

4.2 Algorithm Analysis

As noted in the previous section, the Omega-k algorithm reduces the phase variation in the frequency domain to phase ramps. In this section, it is shown that with a simple modification, the Omega-k algorithm achieves a SNR that, aside from any POSP approximation errors, is the same as that achieved by a matched filter. The matched filter achieves this result by frequency domain multiplication, and the Omega-k algorithm does so by moving the frequency domain signal from one location in the frequency domain to another. This difference in approach has an effect on the focused impulse response which is explored in the following.

4.2.1 Peak SNR

The primary criteria used to define the matched filter in Section 2.1.2 is maximizing the peak SNR. This SNR is achieved when the frequency-domain phase modulation is reduced to phase ramps and the magnitude of the frequency domain signal is squared. The additive white noise is attenuated when the magnitude is squared (see Section 2.1.2). Performing these operations on the frequency domain SAR signal in Equation (2.33) yields

$$\begin{aligned} V(f_\rho, f_z) &= \left| \frac{((f_\rho + f_{\rho 0})^2 - f_z^2)^{\frac{5}{4}}}{r^{\frac{7}{4}}(f_\rho + f_{\rho 0})^3} A\left(\frac{f_z}{\sqrt{(f_\rho + f_{\rho 0})^2 - f_z^2}} \right) \right|^2 H_\rho(f_\rho) \\ & \qquad k e^{-j\frac{\pi}{4}} e^{j\phi_{target}} e^{-j2\pi f_\rho r - j2\pi f_{\rho 0} r - j2\pi f_z z_0}, \end{aligned} \tag{4.4}$$

where $H_\rho(f_\rho)$ is the output of the range matched filter, and the bottom row of terms are the phase ramps and the constant terms unimportant to maximizing the SNR. Evaluating the inverse Fourier transform at the position of the target yields the

integral

$$v(r,z_0) = \frac{k}{r^{\frac{7}{4}}} e^{-j\frac{\pi}{4}} e^{j\phi_{target}} e^{-j2\pi f_{\rho 0} r} \int_{-\infty}^{\infty}\int_{-\infty}^{\infty} H_\rho(f_\rho) \left| \frac{((f_\rho + f_{\rho 0})^2 - f_z^2)^{\frac{5}{4}}}{(f_\rho + f_{\rho 0})^3} A\left(\frac{f_z}{\sqrt{(f_\rho + f_{\rho 0})^2 - f_z^2}}\right)\right|^2 df_\rho df_z, \quad (4.5)$$

where the linear phase ramps are canceled by the exponentials of the inverse Fourier transform.

Next, the output of the Omega-k algorithm at the location of the target is determined. Taking the full frequency domain representation of the signal from Equation (2.33), and performing the Stolt mapping according to Equation (4.2) yields

$$V(\tilde{f}_\rho, f_z) = k\frac{(\tilde{f}_\rho + f_{\rho 0})^{\frac{5}{2}}}{r^{\frac{7}{4}}((\tilde{f}_\rho + f_{\rho 0})^2 + f_z^2)^{\frac{3}{2}}} H_\rho\left(\sqrt{(\tilde{f}_\rho + f_{\rho 0})^2 + f_z^2} - f_{\rho 0}\right) A\left(\frac{f_z}{\tilde{f}_\rho + f_{\rho 0}}\right) e^{-j2\pi \tilde{f}_\rho r - j2\pi f_{\rho 0} r - j2\pi f_z z_0} e^{-j\frac{\pi}{4}} e^{j\phi_{target}}. \quad (4.6)$$

The inverse Fourier transform evaluated at (r, z_0) is

$$v(r,z_0) = \frac{k}{r^{\frac{7}{4}}} e^{-j\frac{\pi}{4}} e^{j\phi_{target}} e^{-2\pi f_{\rho 0} r} \int_{-\infty}^{\infty}\int_{-\infty}^{\infty} H_\rho\left(\sqrt{(\tilde{f}_\rho + f_{\rho 0})^2 - f_z^2} - f_{\rho 0}\right) A\left(\frac{f_z}{\tilde{f}_\rho + f_{\rho 0}}\right) \frac{(\tilde{f}_\rho + f_{\rho 0})^{\frac{5}{2}}}{((\tilde{f}_\rho + f_{\rho 0})^2 + f_z^2)^{\frac{3}{2}}} \frac{|\tilde{f}_\rho + f_{\rho 0}|}{\sqrt{(\tilde{f}_\rho + f_{\rho 0})^2 + f_z^2}} d\tilde{f}_\rho df_z, \quad (4.7)$$

where the last term is the Jacobian term for the change of variables, and the linear phase ramps are canceled by the exponentials of the inverse Fourier transform. To compare this with the output of the ideal matched filter, the change of variables (i.e. Stolt mapping) is reversed to yield the integral

$$v(r,z_0) = \frac{k}{r^{\frac{7}{4}}} e^{-j\frac{\pi}{4}} e^{j\phi_{target}} e^{-2\pi f_{\rho 0} r} \int_{-\infty}^{\infty}\int_{-\infty}^{\infty} H_\rho\left(f_\rho\right) A\left(\frac{f_z}{\sqrt{(f_\rho + f_{\rho 0})^2 - f_z^2}}\right) \frac{((f_\rho + f_{\rho 0})^2 - f_z^2)^{\frac{5}{4}}}{(f_\rho + f_{\rho 0})^3} df_\rho df_z. \quad (4.8)$$

The only difference between this equation and that in Equation (4.5) is the value of the last two terms. Assuming that the antenna window function is known, this integral can be multiplied by

$$A^* \left(\frac{f_z}{\sqrt{(f_\rho + f_{\rho 0})^2 - f_z^2}} \right) \frac{((f_\rho + f_{\rho 0})^2 - f_z^2)^{\frac{5}{4}}}{(f_\rho + f_{\rho 0})^3} \tag{4.9}$$

to make it the same as Equation (4.5). The second term is real and positive for the important values of f_ρ and f_z. The actual modification to the algorithm requires changing Equation (4.7), and the same result is obtained when this equation is multiplied by

$$A^* \left(\frac{f_z}{\tilde{f}_\rho + f_{\rho 0}} \right) \frac{(\tilde{f}_\rho + f_{\rho 0})^{\frac{5}{2}}}{((\tilde{f}_\rho + f_{\rho 0})^2 + f_z^2)^{\frac{3}{2}}}. \tag{4.10}$$

The one modification necessary for the Omega-k algorithm to achieve the same SNR ratio as the matched filter is multiplying the Stolt interpolated signal by Equation (4.10).

While in theory this modification causes the Omega-k algorithm to achieve the same SNR as the matched filter, Equation (4.7) is only an approximate expression. The errors in the POSP approximation of the azimuth Fourier transform reduce the actual peak SNR obtained with this modification. However, when the POSP approximation is accurate, the achieved SNR is valid for targets appearing at all SRCA. This is because the SRCA r only appears as a constant scale term in Equation (4.7).

4.2.2 Stolt Mapping

While the Omega-k algorithm can be modified to achieve a SNR similar to that of the ideal matched filter, the method used to achieve that result is not the same as the matched filter. The matched filter uses frequency domain multiplication, and the Omega-k algorithm moves energy around in the frequency domain. The purpose of this section is to explore the differences between the two resulting point spread functions for SAR systems operating in broadside mode. The effect of system design

parameters on the significance of Stolt mapping is explored, and then the results of two simulations are presented.

4.2.2.1 Effect of Design Parameters and Simulation Setup

As discussed earlier in the chapter, the Stolt mapping shifts energy from the original range frequency f_ρ to the new range frequency $\tilde{f}_\rho$ which is calculated according to

$$\tilde{f}_\rho = \sqrt{(f_{\rho 0} + f_\rho)^2 - f_z^2} - f_{\rho 0}, \tag{4.11}$$

where $f_{\rho 0}$ is the carrier frequency and f_z is the azimuth frequency. The effect of different design choices on the magnitude of the Stolt mapping is explored in two steps: first, the values of f_z and f_ρ which result in the largest shift are identified; then, the effect of the azimuth bandwidth and the radar carrier frequency is developed.

When $f_z = 0$, $\tilde{f}_\rho$ is equal to f_ρ. For other values of f_z, $\tilde{f}_\rho$ is less than f_ρ. While the difference between them is greatest for the maximum value of f_z, that maximum value of f_z varies for different values of f_ρ. From Equation (2.37), $f_{z,max} = (f_\rho + f_{\rho 0}) \sin(\phi_{max})$ where ϕ_{max} is the maximum angle at which the target is seen by the antenna[2]. Using this value for f_z in Equation (4.11) yields

$$\begin{aligned} \tilde{f}_\rho &= \sqrt{(f_\rho + f_{\rho 0})^2 - (f_\rho + f_{\rho 0})^2 \sin^2(\phi_{max})} - f_{\rho 0} \\ &= (f_\rho + f_{\rho 0}) \sqrt{1 - \sin^2(\phi_{max})} - f_{\rho 0} \\ &= (f_\rho + f_{\rho 0}) \cos(\phi_{max}) - f_{\rho 0}, \end{aligned} \tag{4.12}$$

and the difference between f_ρ and $\tilde{f}_\rho$ is

$$\begin{aligned} f_\rho - \tilde{f}_\rho &= f_\rho + f_{\rho 0} - (f_\rho + f_{\rho 0}) \cos(\phi_{max}) \\ &= (f_\rho + f_{\rho 0})(1 - \cos(\phi_{max})). \end{aligned} \tag{4.13}$$

[2]This maximum angle could chosen to be the 3dB angle, but the exact choice is not critical for the discussion.

For a fixed maximum angle, the magnitude of the Stolt shift is greatest for the largest value of f_ρ. Therefore, the Stolt mapping which corresponds to the largest frequency domain shift is

$$\tilde{f}_{\rho,max} = \sqrt{(f_{\rho,max} + f_{\rho 0})^2 - f_{z,max}^2} - f_{\rho 0}, \tag{4.14}$$

where $f_{\rho,max}$ is the maximum range frequency, and $f_{z,max}$ is the corresponding maximum azimuth frequency.

In radar, the significance of a frequency domain shift, e.g. a Doppler shift, on a one dimensional signal depends on bandwidth of the signal–large bandwidth signals are affected less than small bandwidth signals. The Stolt mapping is also a frequency domain shift, and the ratio of the magnitude of the Stolt shift to the range bandwidth

$$\frac{f_{\rho,max} - \tilde{f}_{\rho,max}}{2f_{\rho,max}} = \frac{1}{2}\left(1 - \frac{\tilde{f}_{\rho,max}}{f_{\rho,max}}\right) \tag{4.15}$$

is used to evaluate the significance of the Stolt shift. Substituting Equation (4.14) into Equation (4.15), the ratio becomes

$$\begin{aligned} \frac{1}{2}\left(1 - \frac{\tilde{f}_{\rho,max}}{f_{\rho,max}}\right) &= \frac{1}{2}\left(1 - \frac{1}{f_{\rho,max}}\left(\sqrt{(f_{\rho,max} + f_{\rho 0})^2 - f_{z,max}^2} - f_{\rho 0}\right)\right) \\ &= \frac{1}{2} - \sqrt{\left(\frac{1}{2} + \frac{f_{\rho 0}}{2f_{\rho,max}}\right)^2 - \left(\frac{f_{z,max}}{2f_{\rho,max}}\right)^2} + \frac{f_{\rho 0}}{2f_{\rho,max}}, \end{aligned} \tag{4.16}$$

where an increase in the value of Equation (4.16) is associated with a more significant shift. One important observation is that the actual values of azimuth bandwidth and radar carrier frequency are not important. Instead, it is their value relative to the range bandwidth.

The maximum azimuth frequency $f_{z,max}$ appears in Equation (4.16) only under the radical term, and increasing the ratio of the maximum azimuth frequency to the range bandwidth increases the value of Equation (4.16). The radar carrier frequency, on the other hand, appears in two terms which have opposite effects. The net effect of increasing the radar carrier frequency to range bandwidth ratio is a decrease in the relative magnitude of the Stolt shift as shown in Figure 4.2.

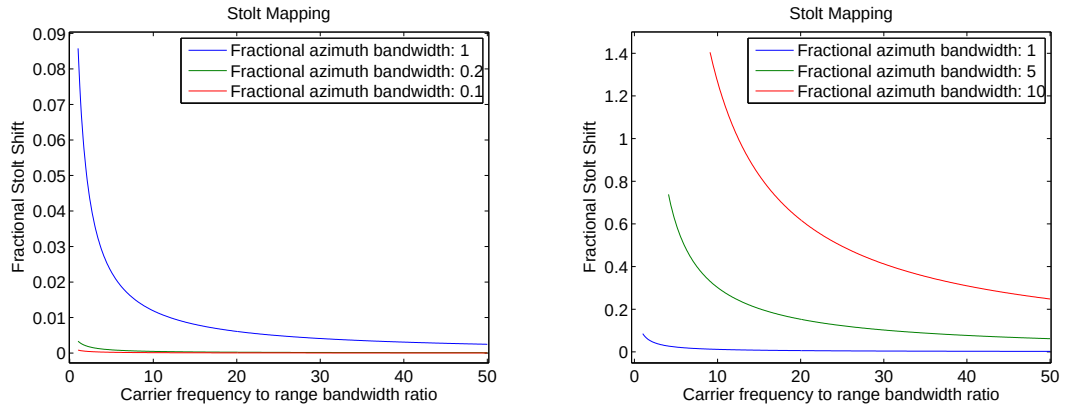

(a) Low azimuth to range bandwidth ratios (b) High azimuth to range bandwidth ratios

Figure 4.2: Plots of the ratio of the largest frequency domain shift to the range bandwidth for various system configurations. The fractional azimuth bandwidth is defined as $f_{z,max}/f_{\rho,max}$, and the fractional Stolt shift is given by Equation (4.16). The frequency domain shift becomes more significant as the radar carrier decreases and the azimuth bandwidth increases (see text).

In summary, the significance of the Stolt mapping is related to two ratios: the ratio of the carrier frequency to the range bandwidth, and the ratio of the azimuth bandwidth to the range bandwidth. For the purposes of comparing two systems, the ratio of the azimuth bandwidth to the range bandwidth is effectively the ratio of the azimuth resolution to the range resolution. This ratio is greater than one for systems with an azimuth resolution which is higher than the range resolution. While the total effect of the Stolt mapping depends on many aspects of the SAR signal (the time-bandwidth product of the range chirp, the actual antenna pattern, etc.), comparing these ratios provides a reasonable starting point for analyzing the significance of the frequency domain shift. In the next section, the results for two simulated SAR signals are presented.

4.2.2.2 Simulation Results

The effect of the Stolt mapping is explored through two simulated SAR signals. The first SAR signal is that of a SAR system with a 500MHz carrier, a 200MHz

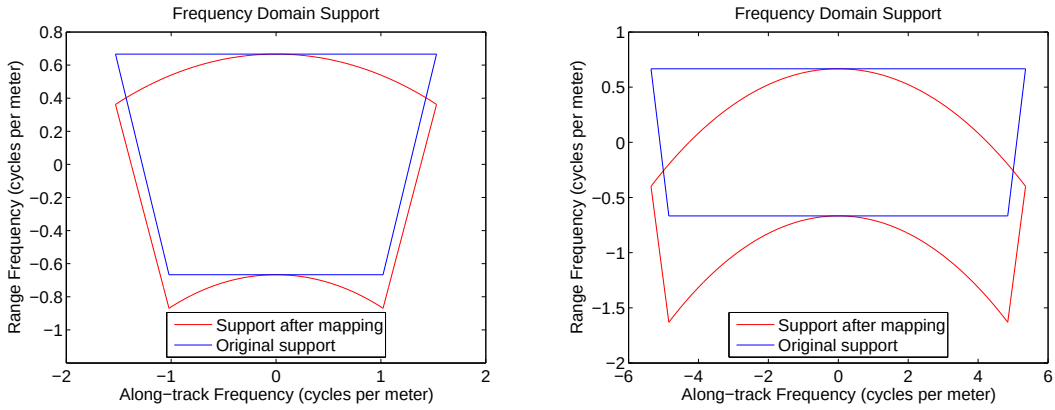

(a) Case one

(b) Case two

Figure 4.3: An illustration of the frequency domain support of the two simulated SAR signals before and after the Stolt mapping. Case one represents a SAR system with a range bandwidth which is a significant fraction of the radar carrier frequency. Case two represents a SAR system with an extremely large azimuth bandwidth and is chosen to emphasize the effect of the Stolt mapping.

range bandwidth, and a 45 degree beamwidth. The carrier to range bandwidth ratio is 2.5 which is rather small, and the azimuth resolution is roughly twice the range resolution. This represent a typical SAR configuration with a relatively low radar carrier frequency. The second SAR signal is that of a SAR system with a 2GHz carrier, a 200MHz range chirp, and a 45 degree beamwidth. The carrier to range bandwidth ratio is ten, and the azimuth resolution is about ten times greater than the range resolution. This second case is more typical of a system designed for multi-look processing. While the entire signal would not normally be processed together to form a single high-resolution image (typically, subaperture processing would performed), it serves to illustrate the effects of the Stolt mapping for an extreme case. Figure 4.3 illustrates the frequency domain shift experienced for each case.

For both cases, the simulated data is processed by the Omega-k algorithm, and the residual frequency domain phase of the signal is removed to avoid including the effect of the POSP approximation errors[3]. The resulting point spread function is

[3]These errors are discussed in Chapter 6.

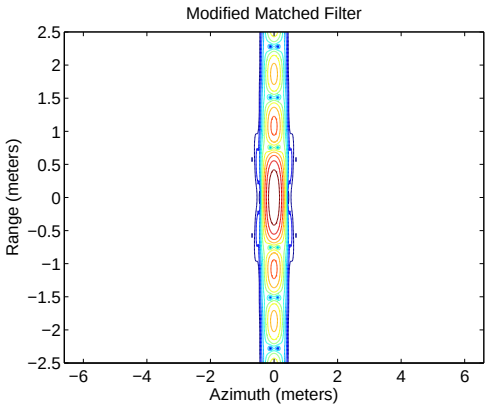

(a) Modified Matched Filter, Case one

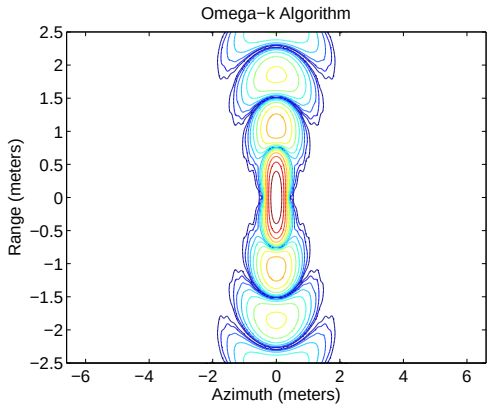

(b) Omega-k, Case one

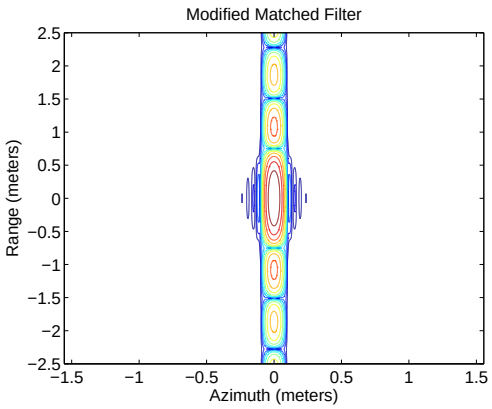

(c) Modified Matched Filter, Case two

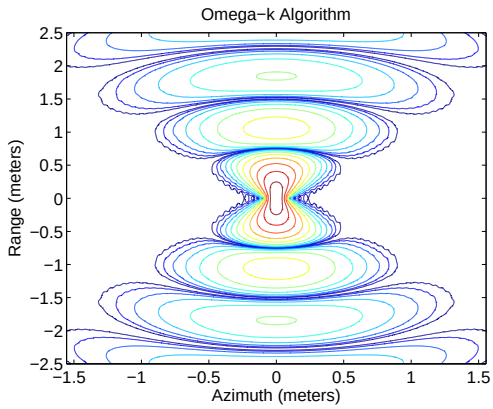

(d) Omega-k, Case two

Figure 4.4: Contour plots of the focused SAR signal for the two simulated, ideal point targets with contours from -5dB to -55dB at 5dB intervals. The plots on the left side show the result of the modified matched filter, and the plots on the right side show the result of using the Omega-k algorithm. In moving energy around in the frequency domain, the Omega-k algorithm causes the range sidelobes to spread out and changes the shape of the main-lobe from an oval to an hour-glass. The effect is quite significant for case two.

compared to the output of a modified version of the matched filter which is obtained by canceling out the frequency domain phase of the raw SAR signal; the magnitude is not squared.

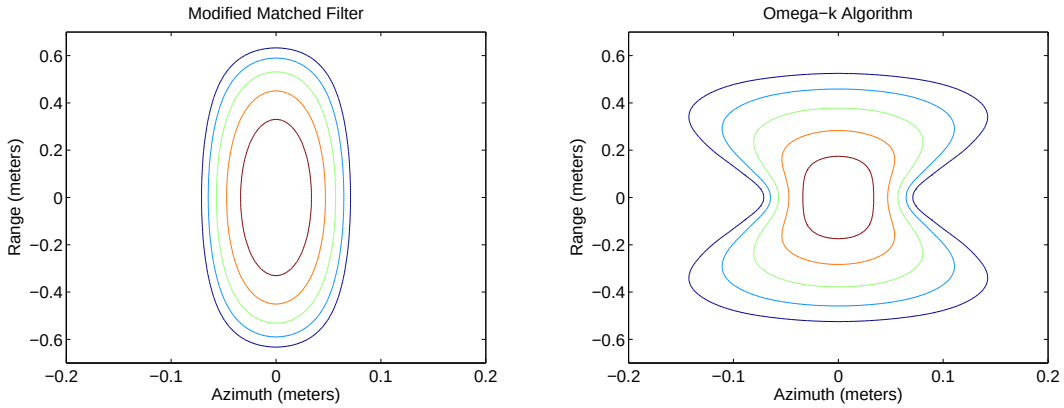

(a) Modified Matched Filter

(b) Omega-k Algorithm

Figure 4.5: Close up contour plots of the main lobe for case two in Figure 4.4 with contours from -3dB to -15dB at 3dB intervals. While the main lobe is quite distorted by the Stolt mapping, the 3db contour (the innermost contour) is really just squared off, and the range resolution is increased by about a factor of two. This improvement comes at the cost of increased interference between scatterers separated in azimuth or separated diagonally.

The effect of the Stolt mapping on magnitude of the resulting time domain signal is shown in Figure 4.4. The most obvious effect of the Stolt mapping is the fanned out range sidelobes, which are also attenuated. For case one, the -55dB contour around the first sidelobe is about three times wider than that observed with the modified matched filter, and the amplitude of the first sidelobe is about 4dB lower. These differences have a fairly significant effect on the interference between nearby scatterers. When the scatterers are separated in range, the decrease in sidelobe amplitude reduces their interference. However, the interference between targets separated diagonally in the image increases.

The magnitude of the main lobe is also spread out. The effect on case one is very slight, but a surprising result is observed for case two. Typically, the 3dB contour of the point spread function defines the system resolution. For case two, the 3dB contour is compressed in range into more of a rectangular shape as shown in Figure 4.5. While the 3dB width in azimuth is largely unaffected by the Stolt

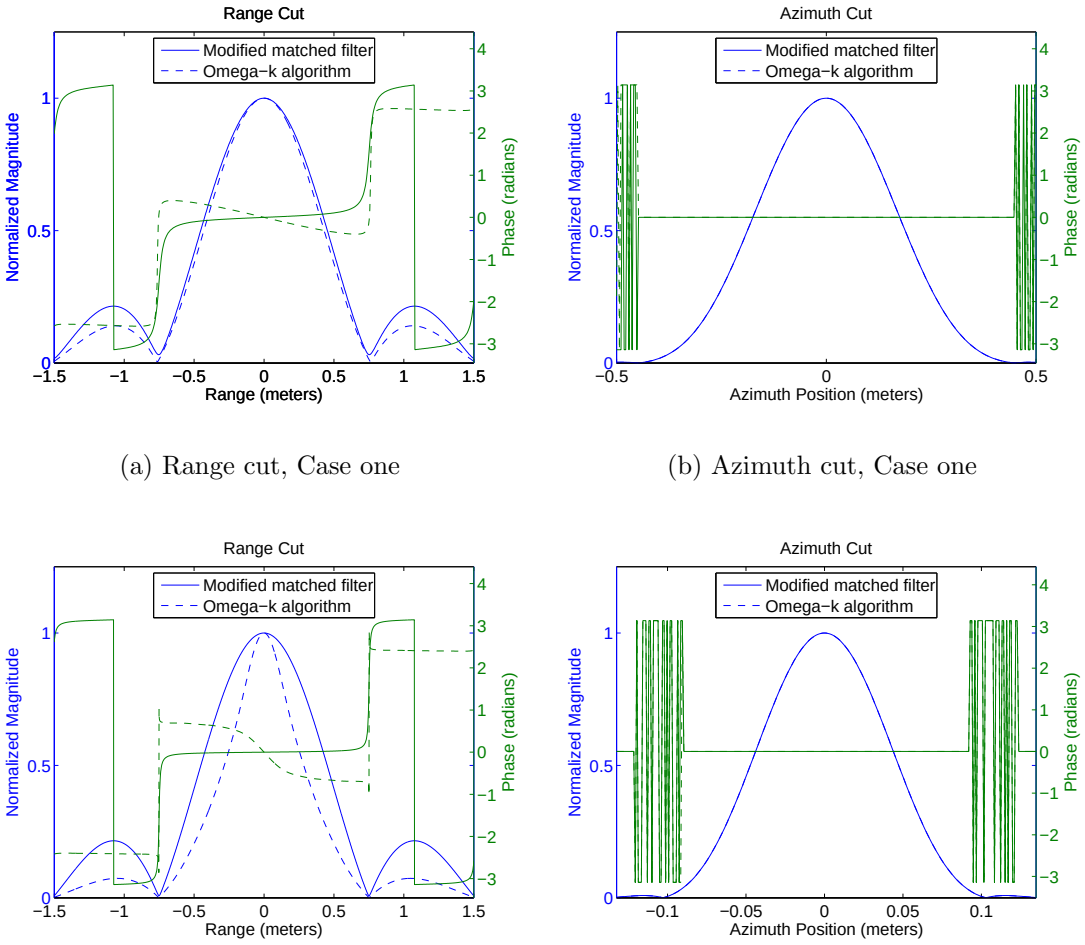

(a) Range cut, Case one

(b) Azimuth cut, Case one

(c) Range cut, Case two

(d) Azimuth cut, Case two

Figure 4.6: Range and azimuth cuts of the focused SAR signal for the two cases in Figure 4.4. In the range direction, the Stolt mapping performed by the Omega-k algorithm decreases the 3dB width and introduces a phase ramp across the main lobe. For case one, the phase variation amounts to a change of about half a radian over the 3dB width. In the azimuth direction, the curves are indistinguishable at this scale.

mapping, the 3dB width in range is reduced by about factor of two. The increased azimuth bandwidth results in an improved range resolution. The improvement does not come without cost. While the 3dB contour is improved in some directions, the main lobe is stretched and more interference is expected for targets which are closely spaced diagonally or closely spaced in azimuth.

Another concern is the effect of the Stolt mapping on the phase of the point spread function. It is noted in [18] that the stability of the phase across the main lobe of the point spread function is important for interferometric SAR systems. While the Stolt mapping reduces the frequency domain phase to constant terms and time delays, the magnitude of the frequency domain signal affects the time-domain phase modulation. For real-valued, two-dimensional frequency domain signals, symmetry through the origin guarantees a real signal. While the collected SAR signal does not exhibit this symmetry, the Stolt mapping further reduces it. For the broadside case considered, the lack of symmetry is isolated to the range direction and results in the phase modulation seen in Figure 4.6. For case one, the phase varies by about half a radian over the 3dB width. For case two, the phase varies by about one radian. Additional research is needed to evaluate the true significance of this phase variation.

4.3 Conclusion

In this chapter, the Omega-k algorithm, with one modification, is shown to achieve the same SNR as the matched filter when the POSP approximation is accurate. It is also shown the frequency domain shift (Stolt mapping) used by the Omega-k algorithm to focus the data alters the resulting point spread function. The differences decrease the potential interference between targets separated in range and increase the potential interference between targets separated in azimuth or diagonally. In addition to the effects observed on the magnitude of the point spread function, the Stolt mapping introduces a noticeable phase modulation across the main lobe which may affect the accuracy of interferometric SAR systems. These effects are explored for two cases, and the means for extending the results to other cases is covered.

Extending the work in this chapter mainly concerns two topics. The first topic is the use of frequency domain window functions to alter the magnitude of sidelobes. For signals with a frequency domain support which is separable in the two dimensions, standard window functions can be applied with predictable results. Unfortunately, the SAR signal is not separable in the two dimensions. Investigations into the effect of various windowing approaches is needed.

The second topic concerns squint-mode SAR systems. The effect of the Stolt mapping on the magnitude of the point spread function is addressed in [1] for squint-mode SAR systems under the assumption that the azimuth bandwidth is much smaller than the mean azimuth frequency. Extending this analysis to also consider the resulting phase may prove important for the squint-mode, interferometric SAR systems. Also, the assumption in [1] that the azimuth bandwidth is much smaller than the mean azimuth frequency breaks down as the azimuth resolution of the squint-mode SAR system is increased, and further investigations into the effect of the Stolt mapping are needed.

Chapter 5

Discrete Time Omega-k Algorithm

While the continuous Omega-k algorithm is useful for analyzing the signal characteristics, it is actually implemented in digital signal processors (DSPs). In many cases, such an implementation is straight-forward. The Omega-k algorithm, however, consists of non-conventional processing techniques in the continuous-time Fourier transform (CTFT) domain, and careful consideration of the relationship between continuous-time signals and their discrete-time counterparts is necessary for proper implementation.

In this chapter, the relationship between continuous-time SAR signals and their discrete-time counterparts is explored. The effect of the differences is addressed for the SAR signal along with a discussion about proper sampling. Then, the discrete-time implementation of the Stolt mapping is considered, and two methods for mixing the frequency domain signal to baseband are compared.

5.1 Discrete-time SAR Signal

To develop the discrete time version of the SAR signal, it is necessary to ensure that sampling does not cause aliasing and to identify any additional phase terms present in the DFT which are not already in Equation (4.1). The topic of aliasing is first addressed for the range direction and then for the azimuth direction. Then, the additional phase terms in the discrete SAR signal are discussed.

5.1.1 Avoiding Aliasing

Aliasing is always a concern with discrete-time processing of continuous-time signals. The necessary steps for avoiding aliasing are considered for both the azimuth and the range direction.

In the range direction, the transmitted signal is typically generated in digital hardware and then passed through a D/A converter. On reception, the analog anti-aliasing filter must sufficiently attenuate any frequencies which alias in the subsequent sampling operation. Strictly speaking, the analog filter used in the D/A converter and the analog anti-aliasing filter must have a finite impulse response to avoid violating the time-finite assumption. Under those conditions, the DFT of the sampled range signal can be viewed as a sampled version of the CTFT of that signal.

In the azimuth direction, the continuous-time signal is sampled by transmitting pulses from specific locations as noted in Section 2.2. A traditional anti-aliasing filter cannot be applied because the azimuth continuous-time signal is never present in the radar system. Fortunately, the antenna pattern serves as a window in both the time and the frequency domains, producing a signal which is approximately finite-length[1] and approximately band-limited. Equation (2.37), provides the relationship between the maximum angle at which energy from a target is collected and the maximum azimuth frequency of the resulting SAR signal.

One approach for sampling the azimuth signal is to choose a threshold such as the 3dB point and to set the sampling rate to avoid aliasing that frequency. The problem with this approach is that the antenna pattern does not roll off very quickly, and there may be significant energy in the sidelobes. Fortunately, as noted in Section 2.3, there is a maximum frequency anticipated in the azimuth direction which is

$$f_{z,max} = (f_{\rho,max} + f_{\rho 0}), \tag{5.1}$$

[1]Strictly speaking, the azimuth signal is not finite-length. The effect of the azimuth segmentation window is addressed in Section 6.3.

where $f_{\rho,max}$ is the maximum spatial frequency associated with the transmitted chirp, and $f_{\rho 0}$ is the radar carrier frequency (again, in cycles per slant-range meter). Sampling at twice this frequency and applying a decimating low-pass filter mitigate the negative effects of aliasing in the azimuth direction. This second approach can be optimized by choosing a lower sampling frequency which only allows aliasing in stop-band of the low-pass filter. This technique is frequently used to relax the transition band requirements on analog anti-aliasing filters [19]. Using either approach, the azimuth signal is sampled without causing significant aliasing.

5.1.2 Matching the Time Origins

Having established that the SAR signal can be digitally sampled without significant aliasing, the last consideration concerns matching the spatial origins. When a continuous time signal is sampled, and a DFT is used to compute the Fourier transform, the first sample needs to correspond to the time origin of the continous-time signal. Otherwise, an additional phase term is introduced.

In the range direction of the SAR signal, the receive delay discussed in Chapter 3 introduces the additional phase term

$$e^{j2\pi f_\rho r_{min}}, \tag{5.2}$$

where r_{min} is the range associated with the first sample. In azimuth, the signal is processed in segments, and the additional phase term is

$$e^{j2\pi f_z z_{seg}}, \tag{5.3}$$

where z_{seg} is the azimuth position corresponding to the beginning of the segment. Incorporating the additional phase terms into the Equation (4.1), the phase of the DFT is a sampled version of:

$$\theta_{2df}(f_\tau, f_\eta) = -2\pi r\sqrt{(f_\rho + f_{\rho 0})^2 - f_z^2} - 2\pi f_z(z_0 - z_{seg}) + 2\pi f_\rho r_{min}. \tag{5.4}$$

In azimuth, the additional phase term places the target in its appropriate location with respect to the start of the segment. For discrete signals, the delays are referenced to the first sample, and the delay of $(z_0 - z_{sig})$ is appropriate for a target located at position z_0. Therefore, nothing needs to be done to the additional phase term in the azimuth dimension.

In range, the additional phase term presents a problem. Left unmodified, the Stolt mapping changes the additional phase term $2\pi f_\rho r_{min}$ into an phase term

$$2\pi \left(\sqrt{(f_\rho + f_{\rho 0})^2 - f_z^2} - f_{\rho 0} \right) r_{min}, \tag{5.5}$$

which alters the resulting point spread function. This additional phase modulation is a function of known parameters and can be removed following the Stolt mapping. Alternatively, the additional phase term $2\pi f_\rho r_{min}$ can be removed prior to applying the Stolt mapping. Either way, the final phase function is

$$-2\pi r \tilde{f_\rho} - 2\pi f_z (z_0 - z_{seg}) - 2\pi r f_{\rho 0}. \tag{5.6}$$

The range delay is also referenced to the first sample, and introducing a phase term $2\pi \tilde{f_\rho} r_{min}$ shifts the targets located at r_{min} to the first range bin. The final expression for the 2-D phase is

$$-2\pi \tilde{f_\rho} (r - r_{min}) - 2\pi f_z (z_0 - z_{seg}) - 2\pi r f_{\rho 0}. \tag{5.7}$$

5.2 Discrete Stolt Mapping

The final consideration for the discrete Omega-k algorithm is the implementation of the Stolt mapping. For the continuous Omega-k algorithm, the process was merely to perform a change of variables. However, the DFT only provides samples of the frequency domain signal. The discrete Stolt mapping must take the samples of Equation (2.33) provided by the DFT, and produce the DFT samples of Equation (5.7).

There are two basic methods for performing the mapping (see [1] and [2]). One approach is to map the DFT samples of f_ρ to the new domain and then interpolate from those samples to the DFT samples of $\tilde{f}_\rho$. This approach is complicated by the fact that the Stolt mapping does not produce uniformly spaced samples in the new domain [2]. The second approach is to determine the values of f_ρ which map to the values of $\tilde{f}_\rho$ associated with the desired DFT samples. The necessary equation is obtained by solving Equation (4.11) for f_ρ to yield

$$f_\rho = \sqrt{(\tilde{f}_{\rho 0} + f_\rho)^2 + f_z^2} - f_{\rho 0}. \tag{5.8}$$

There is a sign ambiguity involved in the development of this equation which is resolved by noting that the important values of $(\tilde{f}_\rho + f_{\rho 0})$ and $(f_\rho + f_{\rho 0})$ are non-negative. Because the DFT samples are uniformly spaced in f_ρ, ensuring proper sampling is easier, and standard interpolation kernels can be used; however, it must be verified that the frequency domain signal is sufficiently sampled.

5.2.1 Satisfying the Frequency Domain Sampling Requirements

The first step in determining the appropriate approach for interpolating the frequency domain signal is to identify the frequency content of that signal. This is done by noting an important relationship for the Fourier transform. Then, two methods for mixing the signal to baseband are compared.

The frequency-domain representation of the signal is obtained with the Fourier transform; however, the difficulty of evaluating that transform is avoided by the observation that applying a Fourier transform twice yields the original signal reversed in time. This is shown by letting $X(f_\rho)$ be the Fourier transform of $x(\rho)$. Then, the

Fourier transform of $X(f_\rho)$ is

$$\begin{aligned}
\int_{-\infty}^{\infty} X(f_\rho) e^{-jf_\rho \rho} df_\rho &= \left[\left[\int_{-\infty}^{\infty} X(f_\rho) e^{-jf_\rho \rho} df_\rho \right]^* \right]^* && (5.9) \\
&= \left[\int_{-\infty}^{\infty} X^*(f_\rho) e^{jf_\rho \rho} df_\rho \right]^* && (5.10) \\
&= [x^*(-\rho)]^* && (5.11) \\
&= x(-\rho). && (5.12)
\end{aligned}$$

Applying this result to the 2-d frequency domain representation of the SAR signal yields $V(-\rho, f_z)$ as the desired Fourier transform. In Chapter 3, it is noted that data is only collected over a set of ranges from r_{min} to some final range which is now referred to as r_{max}. The azimuth Fourier transform does not affect the region of support in range; therefore, the signal in the 2-dimensional frequency domain is band-limited in the range frequency direction between $-r_{max}$ and $-r_{min}$ (units are in meters because it is the frequency content of the frequency domain signal).

The second concern is the sample spacing in the frequency domain. Whenever a DFT is evaluated, the sample spacing in the frequency domain is $1/(NR)$ where N is the number of spatial samples and R is the space-domain sample spacing. Noting that the number of samples N is $((r_{max} - r_{min})/R + 1)$, the frequency domain sample spacing is $1/(r_{max} - r_{min} + R)$. To avoid aliasing the frequency domain signal, the sample spacing must be less than half the period of the largest frequency which is $1/(2r_{max})$, and the Nyquist sampling criteria is satisfied when

$$\frac{1}{r_{max} - r_{min} + R} < \frac{1}{2r_{max}}, \tag{5.13}$$

or, after some simplifications,

$$r_{max} + r_{min} < R. \tag{5.14}$$

In practice, r_{max} and r_{min} are both positive, and their sum is larger than the sample spacing. While the signal is aliased, the complex bandwidth is $r_{max} - r_{min}$, and the

sampling frequency is $r_{max} - r_{min} + R$; the sampling rate is just large enough to avoid destructive aliasing. Thus, the interpolation can be carried out if the signal is mixed up to baseband or an appropriate non-baseband interpolator is used.

Of the two approaches, mixing the signal up to baseband is chosen. This is done by multiplying the frequency domain signal by

$$exp(j2\pi f_\rho r_{mid}), \tag{5.15}$$

where $r_{mid} = (r_{max} + r_{min})/2$. This is the approach taken in [2] for Soumekh's spatial-frequency interpolation method, which is very similar to the Omega-k algorithm. As mentioned earlier, the sample delay introduces a term $exp(j2\pi f_\rho r_{min})$. Instead of removing that term as discussed in the previous section, just adding the term $exp(j2\pi f_\rho (r_{max} - r_{min})/2)$ properly mixes the frequency domain signal to baseband. The actual effect of this modification is to circularly shift the center of the collected data to the first sample as shown in Figure 5.1(b).

5.2.2 Reference Function Multiply

In [1], the frequency domain signal is mixed to baseband through the use of a reference function multiply. The reference function is developed for the situation where both independent variables are time (i.e. fast time in range, and slow time in azimuth). Converting the function to independent variables in position, the phase of the reference function is

$$2\pi r_{ref} \sqrt{(f_\rho + f_{\rho 0})^2 - f_z^2}, \tag{5.16}$$

where r_{ref} is a reference range. Adding this phase term to Equation (4.1) results in a total phase term

$$\theta_{2dfft} = -2\pi (r - r_{ref}) \sqrt{(f_\rho + f_{\rho 0})^2 - f_z^2} - 2\pi f_z (z_0 - z_{seg}). \tag{5.17}$$

Aside from appearing as a constant scaling term in Equation (2.33), the slant range of closest approach (SRCA), r, only factors into the first term of Equation (5.4).

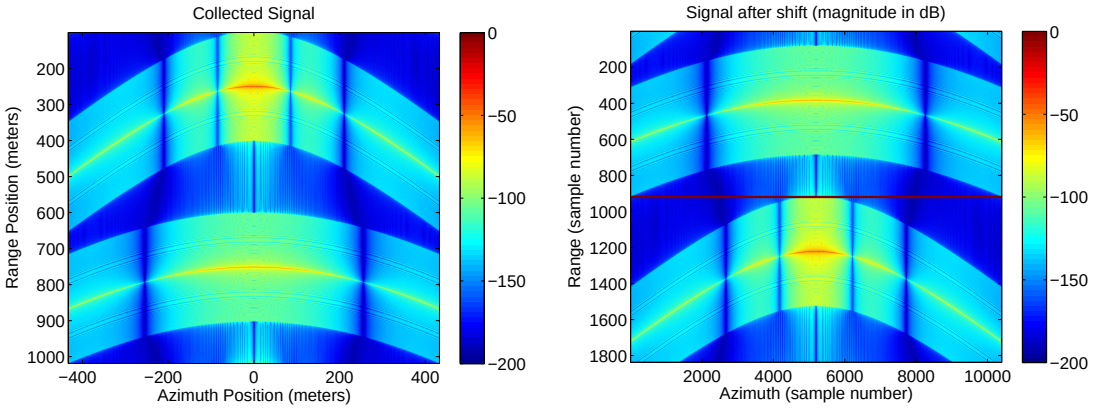

(a) Original signal

(b) Shifted signal

Figure 5.1: The range compressed SAR signal before and after the corresponding frequency domain signal is mixed to baseband. In (a), the top band is the range compressed SAR signal for a target with a SRCA of 250m, and the lower band is the range-compressed SAR signal for a target with a SRCA of 750m. After the frequency domain signal is mixed to baseband, the range-compressed SAR signal is circularly shifted in the range direction. The important observation is that significant energy from a particular target does not cross the center line which is shown in red near range sample 900 in (b).

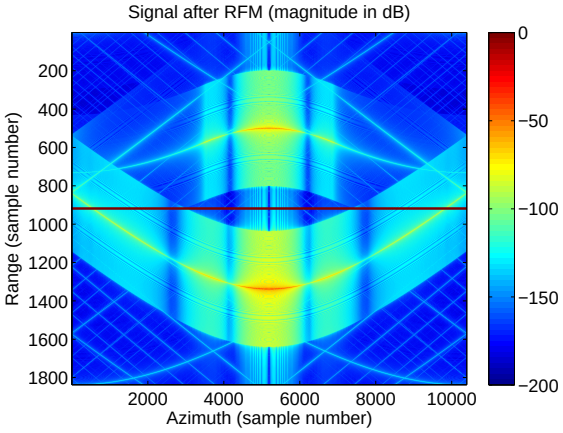

Figure 5.2: The range-compressed signal after the reference function multiply is applied. The RCM of the target in the lower half of the image is backwards because that target appears nearer than the reference range used in the reference function multiply. While some of the energy of that target crosses the red center line, the SAR signal is often filtered in the azimuth direction to eliminate that energy (see text).

In modifying this phase term, the reference function multiply causes the targets to appear as though they are located at a different SRCA. For targets located at r_{ref}, all of the frequency domain phase modulation is removed, and the target is focused in the first range bin at its zero-Doppler position z_0. For targets closer than the reference range, the SRCA becomes negative in the phase term, and the range cell migration (RCM) is changed to occur in the opposite direction, as seen for the target in the bottom half of Figure 5.2. Finally, for targets farther away than the reference range, the RCM is reduced.

Unfortunately, the reference function multiply does not alter the signal in a way which guarantees a baseband signal in the frequency domain. For the frequency domain signal to be baseband, the target energy must not cross the red line in Figure 5.2; however, energy from the near-range target does. Fortunately, this is not typically a problem because the energy which crosses the red line is often filtered out. In Figure 5.1(a), the dark vertical lines in the range compressed signal are associated with the antenna nulls, and the SAR signal is often filtered to eliminate the energy beyond the first null on either side. Considering just the mainlobe portion of the signals in Figure 5.2, there is a significant gap between the two which is actually larger than the same gap observed in Figure 5.1(b).

The difference in the gaps is determined by considering the RCM of the signals. When the circular shift is used to mix the frequency domain signal to baseband, the gap between the two signals is shortened by the RCM of the far-range target. The maximum SRCA at which the signal is collected is $r_{ca,max}$ calculated in Equation (3.3), and the RCM for a target at this range is

$$r_{ca,max}[1/cos(\theta_{max}) - 1], \tag{5.18}$$

where θ_{max} is the maximum angle at which the energy is collected and retained. When the RFM is applied to mix the frequency-domain signal to baseband, this gap is shortened by both the far-range target and the near-range target. The RCM for

the farthest-range target is

$$(r_{ca,max} - r_{ref})[1/cos(\theta_{max}) - 1], \tag{5.19}$$

and the magnitude of the RCM for the nearest-range target is

$$(r_{ref} - r_{ca,min})[1/cos(\theta_{max}) - 1]. \tag{5.20}$$

Adding the terms together result in a combined RCM of

$$(r_{ca,max} - r_{ca,min})[1/cos(\theta_{max}) - 1], \tag{5.21}$$

which is smaller than Equation (5.18) by $r_{ca,min}[1/cos(\theta_{max}) - 1]$. The importance of this difference grows as the minimum SRCA is increased and as the antenna beamwidth is increased. While the magnitude of this gap is not important when the ideal sinc function interpolator is used, a larger gap does reduce the requirements on the frequency domain interpolator. Additional research into the effect of non-ideal interpolators on the resulting point spread function is needed.

While the size of the gap is maintained as long as r_{ref} falls between $r_{ca,min}$ and $r_{ca,max}$, the placement of the gap is important to prepare the frequency domain signal for interpolation. Choosing r_{ref} to be half way between $r_{ca,min}$ and $r_{ca,max}$ centers the gap in the image. This minimizes the aliasing for targets between the maximum and minimum ranges.

5.2.3 Interpolator

The analysis up to this point establishes the methods for properly digitizing the SAR signal and for preparing the frequency domain signal for interpolation. The last concern is the choice of interpolating kernel. When the signal is mixed to baseband either by the shift or by the RFM, the ideal interpolator is a sinc function interpolator

of the form

$$\sum_{n=0}^{N-1} \frac{\sin\left(\pi r_{swath}(f_{\rho,n} - f_{\rho,new})\right)}{\pi r_{swath}(f_{\rho,n} - f_{\rho,new})} V(f_{\rho,n}, f_z), \tag{5.22}$$

where $r_{swath} = r_{max} - r_{min}$, $f_{\rho,n}$ is the range frequency associated with the nth DFT sample in f_ρ, and $f_{\rho,new}$ is the value of f_ρ which maps to the desired DFT sample in $\tilde{f}_\rho$. This interpolator is appropriate because the DFT samples are samples of the continuous frequency domain signal.

5.3 Final Consideration

The final consideration concerns the interpolated frequency domain array. The Stolt mapping shifts the frequency domain signal towards negative f_ρ as shown in Figure 4.1. When the range oversampling is not sufficient to contain the mapped signal, it is necessary to increase the size of the frequency domain arrays. The minimum range frequency is calculated according to

$$\tilde{f}_{\rho,min} = \sqrt{(f_{\rho,min} + f_{\rho 0})^2 - f_{z,min}^2} - f_{\rho 0}, \tag{5.23}$$

where $f_{\rho,min}$ is the smallest range frequency at which significant energy is present, and $f_{z,min}$ is the calculated according to

$$f_{z,min} = (f_{\rho,min} + f_{\rho 0}) cos(\phi_{max}), \tag{5.24}$$

and ϕ_{max} is the maximum angle at which signal energy is received. The sample spacing in the new frequency domain array should be kept the same as the original sample spacing in f_ρ.

5.4 Algorithm Summary

When using the reference function multiply from [1], the final discrete Omega-k algorithm is

1. Filter and decimate the SAR signal in the azimuth direction.

2. Perform a two-dimensional FFT on the range-compressed SAR data.

3. Create an additional frequency domain array which is large enough to contain the new values of $\tilde{f}_\rho$ (see Equation (5.23)). The frequency domain sample spacing for the new array is kept the same as the original frequency domain sample spacing for the range-compressed SAR signal, but is extended in size. This is sometimes known as spectral extension.

4. Remove the phase term associated with the receive delay by multiplying the frequency domain signal by $exp(-j2\pi f_\rho r_{min})$.

5. Perform the reference function multiply by multiplying the frequency domain signal by $exp(j2\pi r_{ref}\sqrt{(f_\rho + f_{\rho 0})^2 - f_z^2})$, where r_{ref} is half way between the values of $r_{ca,min}$ and $r_{ca,max}$ discussed in Chapter 3.

6. Calculate the values of f_ρ which are associated with each DFT samples in $\tilde{f}_\rho$, and interpolate the signal to those values using Equation (5.22).

7. Calculate the inverse FFT of the interpolated frequency domain data.

5.5 Conclusion

In this chapter, the details of a discrete implementation of the Omega-k algorithm are explored. The issues associated with aliasing the time-domain SAR signal is discussed along with the effect of the receive delay. Implementing the Stolt mapping on the DFT samples requires interpolation in the frequency domain, and two methods for mixing the frequency domain signal to baseband are compared. While the reference function multiply used in [1] does not guarantee that aliasing in the frequency domain signal is avoided, it does have the potential for reducing the requirements on the frequency domain interpolator. Additional research is needed to quantify the effect of a non-ideal interpolator.

Chapter 6

POSP Approximation

The key approximation used in the development of the frequency domain representation of the SAR signal is the principle of stationary phase (POSP) approximation. As with every approximation, it is important to understand the nature of the approximation error. In the case of SAR, this error is of particular importance because the Omega-k algorithm uses the resulting expression for the phase to process the data, and any approximation errors directly affect the ability of the algorithm to produce properly focused SAR images.

The topic of the POSP approximation is introduced in many books on SAR, notably [1], [3], and [2]. In those references, the POSP approximation is motivated; however, the actual errors observed are only lightly covered. In this chapter, a short tutorial on the POSP approximation is presented. Then, through the use of a simple example, insight is gained into the approximation error, and the analysis is extended to more general integrals. The insight gained is then used to analyze the azimuth Fourier transform of the SAR signal. Finally, the approximation errors are explored through simulation.

6.1 Principle of Stationary Phase

The principle of stationary phase is one of the methods used to arrive at a closed form expression for integrals without a known closed-form solution and applies to integrals of the form

$$\int_a^b f(x)e^{j\lambda g(x)}dx, \tag{6.1}$$

where λ is a constant real number. The most common method for employing the principle of stationary phase is to find the point x_{sp} such that $g'(x_{sp})$ is zero (i.e. the

stationary phase point). Then, $f(x)$ is approximated by $f(x_{sp})$ and $g(x)$ is approximated by a second order Taylor expansion around the stationary phase point(s) [20]. When the integral limits are finite, a closed form solution is obtained by pushing out the limits to infinity.

We are only concerned with functions $g(x)$ which have a single stationary phase point. Under that assumption, the actual steps of the POSP approximation can be carried out prior to knowing the functions $f(x)$ and $g(x)$. The important approximations are

$$f(x) \approx f(x_{sp}) \tag{6.2}$$

and

$$g(x) \approx g(x_{sp}) + 0.5g''(x_{sp})(x - x_{sp})^2. \tag{6.3}$$

Substituting these approximations in the integral yields

$$\begin{aligned} \int_a^b f(x)e^{j\lambda g(x)}dx &\approx \int_a^b f(x_{sp})e^{j\lambda[g(x_{sp})+\frac{1}{2}g''(x_{sp})(x-x_{sp})^2]}dx \\ &= f(x_{sp})e^{j\lambda g(x_{sp})}\int_a^b e^{j\frac{1}{2}\lambda g''(x_{sp})(x-x_{sp})^2}dx \\ &\approx f(x_{sp})e^{j\lambda g(x_{sp})}\int_{-\infty}^{\infty} e^{j\frac{1}{2}\lambda g''(x_{sp})(x-x_{sp})^2}dx. \end{aligned} \tag{6.4}$$

Performing a change of variables according to $y = x - x_{sp}$ yields

$$\begin{aligned} \int_a^b f(x)e^{j\lambda g(x)}dx &\approx f(x_{sp})e^{j\lambda g(x_{sp})}\int_{-\infty}^{\infty} e^{j\frac{1}{2}\lambda g''(x_{sp})y^2}dy \\ &= f(x_{sp})e^{j\lambda g(x_{sp})}e^{jsgn(\lambda g''(x_{sp}))\frac{\pi}{4}}\sqrt{\frac{2\pi}{|\lambda g''(x_{sp})|}}, \end{aligned} \tag{6.5}$$

where the last step is performed using[1]

$$\int_{-\infty}^{\infty} e^{j\lambda x^2}dx = e^{jsgn(\lambda)\frac{\pi}{4}}\sqrt{\frac{\pi}{|\lambda|}}, \tag{6.6}$$

[1]The result can be obtained by using the first relation on pg. 395 of [21] separately for the real and imaginary parts of the integral.

and $sgn(\cdot)$ returns the sign of the argument. Applying the POSP approximation to a particular integral requires identifying $f(x)$ and $\lambda g(x)$ and plugging the necessary values into Equation (6.5).

In the discussion which follows, the POSP approximation is motivated by considering the Fourier transform of a linear FM chirp, and the errors are addressed. This analysis is then extended by considering the approximation errors encountered with more general integrals.

6.1.1 Linear FM Chirps

A common waveform for radar systems is the linear FM chirp; however, the Fourier transform of the linear FM chirp

$$\int_{-\infty}^{\infty} rect\left(\frac{x}{T}\right) e^{j\lambda x^2} e^{-j2\pi f_x x} dx = \int_{-\frac{T}{2}}^{\frac{T}{2}} e^{j\lambda x^2} e^{-j2\pi f_x x} dx \tag{6.7}$$

does not have a known closed-form solution. Given values for λ and T, the integral could be evaluated numerically, but the result is only applicable to those values. The POSP approximation provides a means of obtaining an approximate closed-form solution. In this section, the POSP approximation is applied to Equation (6.7), and the source and magnitude of the errors are explored.

Applying the POSP approximation to the Fourier transform integral requires that the necessary functions be identified. From Equation (6.7),

$$f(x) = rect\left(\frac{x}{T}\right), \tag{6.8}$$

and

$$g(x) = \lambda x^2 - 2\pi f_x x. \tag{6.9}$$

The necessary derivatives of $g(x)$ are

$$g'(x) = 2\lambda x - 2\pi f_x \tag{6.10}$$

and

$$g''(x) = 2\lambda. \tag{6.11}$$

The stationary phase point is found by setting Equation (6.10) equal to zero and solving for x to yield

$$x_{sp} = \frac{\pi f_x}{\lambda}. \tag{6.12}$$

Finally, the second order Taylor expansion of $g(x)$ is determined from Equation (6.9), Equation (6.10), and Equation (6.11) to be

$$g(x) = -\frac{\pi^2 f_x^2}{\lambda} + \lambda \left(x - \frac{\pi f_x}{\lambda} \right)^2, \tag{6.13}$$

which is an exact expression for $g(x)$. The result of the POSP approximation is obtained by inserting the appropriate terms into Equation (6.5) to yield

$$\int_{-\infty}^{\infty} rect\left(\frac{x}{T}\right) e^{j\lambda x^2} e^{-j2\pi f_x x} dx \approx rect\left(\frac{\pi f_x}{T\lambda}\right) e^{-j\frac{\pi^2 f_x^2}{\lambda}} e^{sgn(\lambda)\frac{\pi}{4}} \sqrt{\frac{2\pi}{|\lambda|}}, \tag{6.14}$$

which is the POSP approximation of Equation (6.7). The benefit is that Equation (6.14) provides an answer that can easily be evaluated for any combination of λ and T. The validity of the approximation, however, is not immediately clear.

The validity of the POSP approximation is evaluated by considering the nature of the integrand. The imaginary part of a linear FM chirp is shown in Figure 6.1(a). As the distance from the stationary phase point increases, each oscillation looks more and more like one period of a sinusoid. This is because the change in instantaneous frequency over one oscillation becomes smaller and smaller. As a result, the contribution of each oscillation to the value of the integral drops off very quickly as shown in Figure 6.1(b).

The actual integrand for $f_z = 0$ is a windowed linear FM chirp like the one shown in Figure 6.2(a). While the actual integrand is limited by the rect, the POSP approximation ignores the limits imposed by the *rect*, and integrates the linear FM signal over all time. The resulting error in the approximation is caused by two sources:

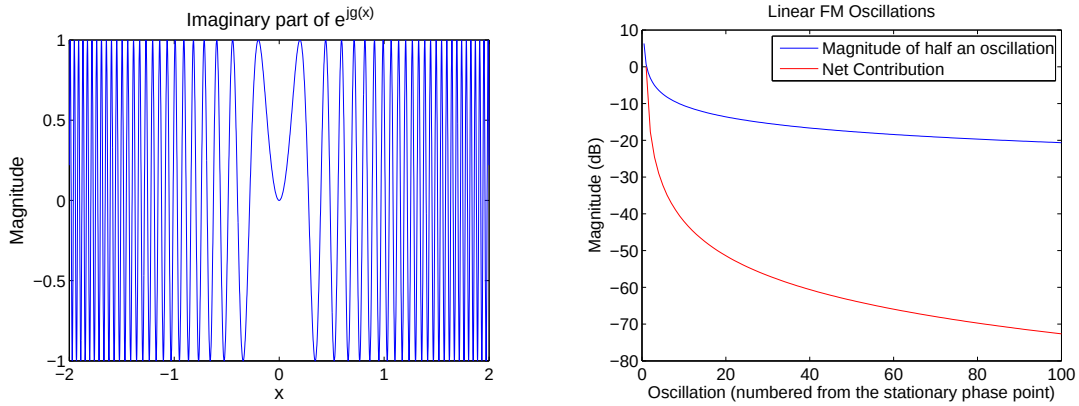

(a) Imaginary part of the linear FM chirp.

(b) Magnitude of the contribution of each oscillation, normalized by the contribution of the first full oscillation.

Figure 6.1: Plots of linear FM chirp with $\lambda = 40$. From (b), the most significant contribution to the integral of the linear FM chirp is from the region immediately around the stationary phase point.

the partial oscillations located just outside the rect and the infinite sum of complete oscillations outside of the rect. The relative magnitude of the two sources of error depends on the actual values of λ and T.

As the Fourier transform is evaluated larger values of f_x, the stationary phase point is shifted closer to one edge of the *rect* as shown in Figure 6.2. This shift changes the POSP approximation error by altering both the number of complete oscillations and the portion of the final oscillation which fall within the *rect*. The effect of the partial oscillation is considered separately from the complete oscillations because the contribution of half an oscillation is much more significant than a complete oscillation (see Figure 6.1(b)). Also, each complete oscillation which goes from being inside the *rect* to being outside the *rect* is a partial oscillation, and the magnitude of its contribution fluctuates substantially during the transition.

The actual effect of the fluctuations is a combination of the effects from the partial oscillations on either side of the *rect*; however, the partial oscillation closest to the stationary phase point has a larger peak magnitude. Thus, the magnitude

of the fluctuation in the POSP error is expected to increase as the stationary phase point is moved closer to the edge. These effects are observed for both the real and the imaginary parts of the signal, but the oscillations for the real part of the signal are 90 degrees out of phase from the imaginary part. This difference causes the phase of the error to fluctuate as well.

Once the stationary phase point is moved just beyond the edge of the rect, the POSP approximation predicts zero magnitude. While the magnitude does not immediately drop to zero for the value of f_x which places the stationary phase point at the edge of the rect, a little more can be said. When the actual integral is evaluated for $f_x = 0$, the most significant oscillations near the stationary phase point appear on both sides. When the stationary phase point is moved to the edge of the rect, only half of those oscillations fall inside the *rect*. There are additional oscillations, but their magnitude is not as significant as those closest to the stationary phase point. Therefore, the magnitude of the Fourier transform at the value of f_x which places the stationary phase point on the edge of the rect is approximately the 6dB point.

These effects are shown through simulation. For the simulation, a linear FM chirp is oversampled by a factor of 10 to sufficiently reduce the effect of aliasing. Then, the Fourier transform is obtained by taking an FFT. The difference between the predicted phase and the actual phase is shown in Figure 6.3 along with a scaled plot of the magnitude. One possible application of the POSP approximation is the development of a matched filter in the frequency domain. The difference between the predicted magnitude and the actual magnitude means the frequency domain signal cannot be squared as necessary for the matched filter. Furthermore, using the POSP approximation does not fully cancel out the phase of the frequency domain signal. While the constant value of the residual phase changes the phase of the resulting time-domain signal, the phase fluctuations affect the peak magnitude, the phase at the peak, and the shape of the resulting time domain signal.

The magnitude of these errors is determined by the number of oscillations present in the signal when the stationary phase point is centered in the *rect* (see Figure 6.1(b)). An important point is that the net area under one oscillation relative

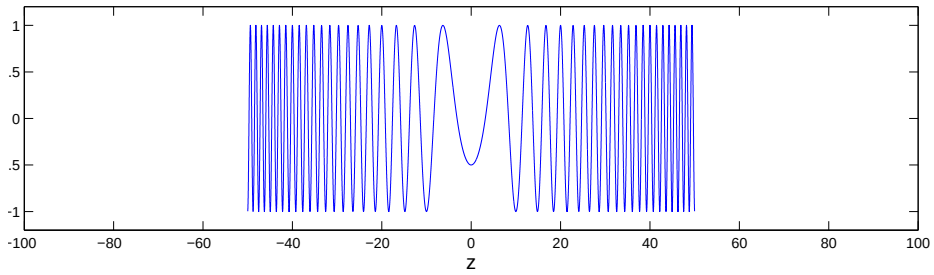

(a) $f_z = 0$

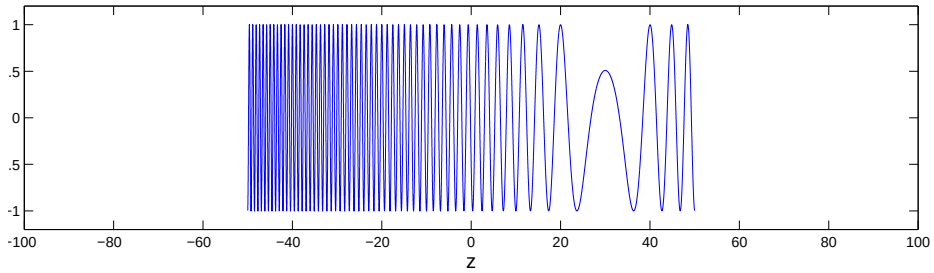

(b) Positive f_z

Figure 6.2: Plots of the actual integrand for the Fourier transform of a linear FM chirp at two values of f_z. The POSP approximation ignores the limits imposed by the *rect* and integrates the function over all time. As the stationary phase point is moved closer to the edge, the additional oscillations included in the approximation become more significant and reduce the accuracy of the POSP approximation.

to that of another does not vary with λ. This is shown by considering the integral of the real part of the linear FM chirp $exp(j\lambda_1 x^2)$ which is $cos(\lambda_1 x^2)$. Starting the first oscillation at stationary phase point $x = 0$ and to proceeding in the positive x direction, oscillation n ends at

$$x = \sqrt{\frac{n2\pi}{\lambda_1}}, \tag{6.15}$$

where $n = 1$ corresponds with the first oscillation. The magnitude of the contribution for the nth oscillation is

$$\int_{\sqrt{\frac{(n-1)2\pi}{\lambda_1}}}^{\sqrt{\frac{n2\pi}{\lambda_1}}} cos(\lambda_1 x^2) dx. \tag{6.16}$$

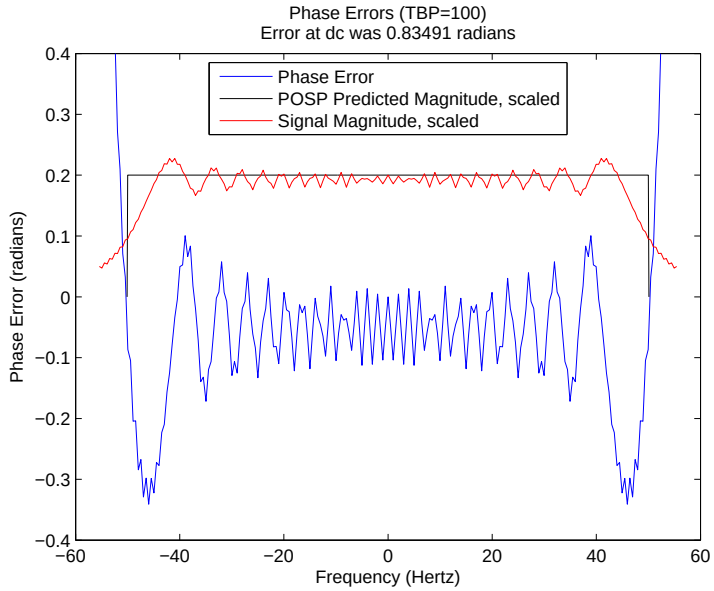

Figure 6.3: Plots showing the POSP error for a linear FM chirp with a time-bandwidth product of 100. The fluctuation in the error caused by the partial oscillations at the edges of the rect are very evident. The red curve is the scaled magnitude of the Fourier transform and is included for reference.

This integral can be compared to that of another linear FM chirp by performing a change of variables according to $y = x\sqrt{\lambda_1/\lambda_2}$. The resulting integral, which is equivalent to Equation (6.16), is

$$\sqrt{\frac{\lambda_2}{\lambda_1}} \int_{\sqrt{\frac{(n-1)2\pi}{\lambda_2}}}^{\sqrt{\frac{n2\pi}{\lambda_2}}} cos(\lambda_2 y^2) dy, \tag{6.17}$$

where the integral is the contribution of the nth oscillation of a linear FM chirp with a chirp rate of λ_2. The important observation is that the relative magnitude of the oscillations remains the same because the scale factor scales each contribution equally. The same is true for the imaginary part of the chirp and is seen by replacing cos with sin in the above integrals.

Thus the number of oscillations present in the actual linear FM chirp is a consistent metric for evaluating the POSP approximation error regardless of the value of λ. As noted in [1], the time-bandwidth product is exactly four times the number

of oscillations present in the actual integrand when the stationary phase point is centered in the *rect*, and the time-bandwidth product is an equivalent criteria. In general, the POSP approximation is considered accurate for linear FM chirps with a time-bandwidth product greater than 100 [1].

In previous discussion, baseband chirps have been assumed. Extending the analysis to non-baseband chirps is straight-forward. For these chirps, the spectrum is mixed up to a higher center frequency which is equal to the value of f_x which places the stationary phase point in the center of the *rect*.

6.1.2 More General Integrals

Applying the POSP approximation to more general functions introduces two additional sources of error. The first arises when $g(x)$ is not quadratic, and the second is introduced when $f(x)$ is not constant. With respect to these errors, conditions under which the POSP approximation is most accurate are identified.

When $g(x)$ is not quadratic, the second order Taylor approximation has the potential of introducing additional error. This error depends directly on how well $g(x)$ is approximated by the quadratic function; however, it is most significant around the stationary phase point. Thus, the approximation is most accurate for cases where the quadratic approximation is valid until the oscillations for both the actual function and the quadratic approximation become insignificant.

When $f(x)$ is not constant, the actual contribution of each oscillation changes. Assuming that the quadratic approximation of $g(x)$ is sufficiently accurate, the linear term of $f(x)$ does not contribute anything. This is because multiplying the symmetric quadratic phase function by a linear function results in an anti-symmetric function, and the integral over any finite symmetric interval is zero. Therefore, when $f(x)$ is sufficiently linear around the stationary phase point, the constant approximation of $f(x)$ captures the contribution in that area. It may be possible to contrive cases where the later oscillations are rendered significant; however, in general, the POSP approximation is most accurate when $f(x)$ varies slowly in comparison to $exp(jg(x))$ (see also [20]).

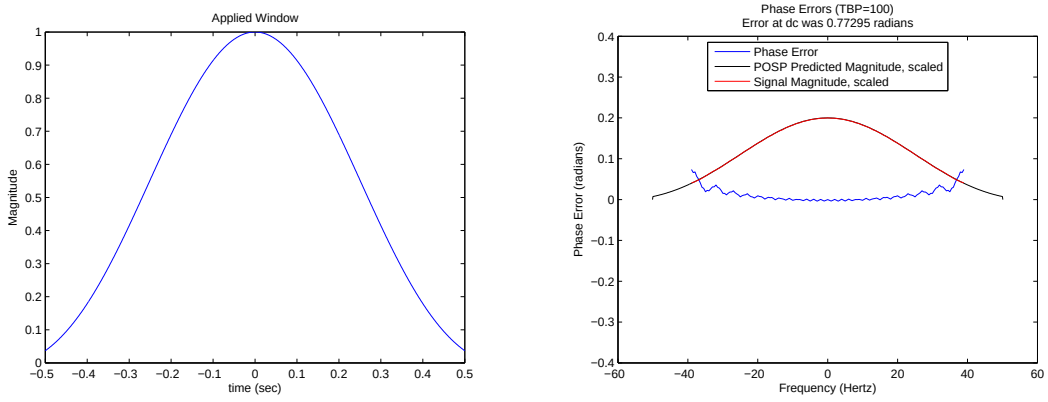

(a) Windowing function

(b) Resulting phase error

Figure 6.4: A Kaiser window function used to window the same linear FM chirp used in Figure 6.3 and the resulting frequency domain phase error. When the linear FM chirp is windowed by this Kaiser window instead of a *rect*, the partial oscillations at the edges of the window are much smaller. This difference significantly reduces the variation of the frequency domain phase errors associated with the POSP approximation, and the actual magnitude is almost indistinguishable from the predicted magnitude. The gradual trend in the phase error is most likely due to the shape of the window function as the trend is not seen in Figure 6.3.

The last scenario to be considered is the case where $f(x)$ has finite support in x but is tapered at the edges. The most notable difference between this scenario and one where $f(x)$ exhibits a discontinuity is the reduction in the magnitude of the partial oscillations near the edge of the $f(x)$. As an example, a Kaiser window is applied to the linear FM chirp used for Figure 6.3 and the resulting variation in the phase error is shown in Figure 6.4. The first difference between this error and that seen in Figure 6.3 is the magnitude of the oscillations in the phase error. This difference is attributed to the decreased magnitude of the discontinuity. The second difference is the introduction of an approximately quadratic phase error attributed to the non-linear variation of the Kaiser window.

Summarizing these ideas, the POSP approximation is most accurate when $g(x)$ is approximately quadratic while the resulting oscillations are significant, and $f(x)$ varies slowly with respect to $exp(jg(x))$. When $f(x)$ has finite support in x (as

with most practical cases), smaller discontinuities lead to smaller oscillations in the frequency domain phase errors.

6.2 Azimuth Fourier Transform

In many aspects of engineering, the design of the system plays a large part in the details of the mathematical relationships, and identifying the effect of system parameters provides the foundation for making good design decisions. As discussed in the previous section, the aspects of the signal relevant to the POSP approximation are the errors in the quadratic approximation of $g(x)$, the time-bandwidth product, and the shape of $f(x)$. The effect of the various design parameters on these aspects of the SAR signal are explored in the context of the azimuth Fourier transform.

The first steps in performing this analysis are determining the equation for the azimuth Fourier transform and identifying the necessary functions. The SAR signal is 2D, and the azimuth Fourier transform is considered after the range Fourier transform is performed. Theoretically, the order is not important; however, proceeding in this order results in an integral to which the POSP approximation can easily be applied. After the range Fourier transform, the signal in Equation (2.32) is obtained, and the azimuth Fourier transform of that signal is

$$\begin{aligned} V(f_\rho, f_z) &= H_\rho(f_\rho) e^{j\phi_{target}} \int_{-\infty}^{\infty} \frac{1}{\left[(z-z_0)^2 + r^2\right]^2} A\left(\frac{z-z_0}{r}\right) \\ &\qquad e^{-j2\pi(f_\rho + f_{\rho 0})\sqrt{r^2+(z-z_0)^2}} e^{-j2\pi f_z z} dz, \end{aligned} \tag{6.18}$$

where $H_\rho(f_\rho)$ is a real valued window function corresponding to the matched-filtered range chirp. The functions for the POSP approximation of the integral are

$$f(z) = \frac{1}{\left[(z-z_0)^2 + r^2\right]^2} A\left(\frac{z-z_0}{r}\right) \tag{6.19}$$

and

$$g(z) = -2\pi \left[(f_\rho + f_{\rho 0})\sqrt{r^2 + (z-z_0)^2} + f_z z)\right]. \tag{6.20}$$

The frequency domain expression for this integral is obtained by applying the POSP approximation in the standard way (i.e. $f(x)$ is approximated by a zeroth order Taylor approximation and $g(x)$ by a second order Taylor approximation). The details of the derivation are a little more involved than those for the linear FM chirp and are carried out in Appendix A. The purpose of this section is to address the factors which influence the accuracy of the approximation, and to identify the ways in which design parameters can be chosen to reduce the POSP approximation error.

6.2.1 POSP Approximation Errors

The effect of system design parameters is considered for three aspects of the SAR signal which affect the POSP approximation error. These three aspects are the time-bandwidth product of the integrand, the accuracy of a quadratic approximation of Equation (6.20), and the shape of $f(z)$. Each of these aspects are considered independently for broadside SAR systems.

The first aspect of the SAR signal concerns the quadratic approximation of $g(z)$. To clearly illustrate the effect of the design parameters on the approximation error, the analysis is restricted to the case where $f_z = 0$. For this case, the actual phase term is

$$-2\pi(f_\rho + f_{\rho 0})\sqrt{r^2 + (z - z_0)^2} = -2\pi(f_\rho + f_{\rho 0})r\sqrt{1 + \frac{(z - z_0)^2}{r^2}}, \tag{6.21}$$

and the phase term used in the approximation is

$$-2\pi(f_\rho + f_{\rho 0})r\left(1 + \frac{(z - z_0)^2}{2r^2}\right). \tag{6.22}$$

The term inside the parentheses in Equation (6.22) is always positive and the equation can be written as

$$-2\pi(f_\rho + f_{\rho 0})r\sqrt{1 + \frac{(z - z_0)^2}{r^2} + \frac{(z - z_0)^4}{r^4}}. \tag{6.23}$$

Comparing Equation (6.23) to Equation (6.21), the only difference is the final quartic term which happens to be the tangent of the angle to the target raised to the fourth power. For SAR systems operating in broadside mode, the beamwidth limits the magnitude of that angle, and larger beamwidths increase the error in the square-root term. The other variables, namely $(f_\rho + f_{\rho 0})$ and r, scale that error term, and larger values of either quantity also increase the maximum error.

Next, the effect of the design parameters on the time-bandwidth product is explored. Designating z_{max} as the largest value of $(z - z_0)$ which is included in the antenna beamwidth, the corresponding instantaneous frequency, from the first derivative of Equation (6.21), is

$$(f_\rho + f_{\rho 0}) z_{max} \frac{1}{\sqrt{r^2 + z_{max}^2}}. \tag{6.24}$$

For baseband chirps (broadside SAR), the bandwidth is approximately twice that highest frequency, and the length is $2z_{max}$. Multiplying those quantities, the time-bandwidth product is

$$4(f_\rho + f_{\rho 0}) z_{max}^2 \frac{1}{\sqrt{r^2 + z_{max}^2}} = 4(f_\rho + f_{\rho 0}) r \frac{z_{max}^2/r^2}{\sqrt{1 + z_{max}^2/r^2}}. \tag{6.25}$$

The value of the last term in Equation (6.25) is entirely determined by the antenna beamwidth, and increasing the beamwidth increases the time-bandwidth product. When the beamwidth is held constant, larger values of $(f_\rho + f_{\rho 0})$ and r also increase the resulting time-bandwidth product. An important observation is that *changing the radar design parameters in a way which increases the time-bandwidth product also increases the error in the quadratic approximation of* $g(z)$.

The final consideration is the shape of $f(z)$. The first term in Equation (6.19) is due to the linear trajectory traced out by the SAR sensor. That term is fixed for stripmap SAR systems, and causes a fairly gradual variation in the amplitude. The second term is the window function due to the antenna pattern. Fortunately, typical antenna patterns have relatively smooth magnitude responses and do not

support discontinuities. While the actual effect is specific to each antenna, choosing antennas with a smooth variation over the main lobe is expected to decrease the POSP approximation error.

While the antenna pattern does not introduce discontinuities, the implicit window introduced when the data is processed does. As discussed in Section 3.2, the data is typically segmented in the azimuth direction for processing. This introduces an additional window into $f(z)$ that has the potential of creating a significant discontinuity. The discontinuity is most significant for targets located near the edge of the segment where the segment window cuts into the main lobe of antenna window function.

The three aspects of the SAR signal which affect the POSP approximation error are the time-bandwidth product, the accuracy of the quadratic approximation of the phase function, and the shape of $f(z)$. Values of $(f_\rho + f_{\rho 0})$, r, and the beamwidth can be changed to increase the time-bandwidth product. That change, however increases the error in the quadratic approximation of the time-domain phase function. Without a closed form expression for the effect of those changes, the actual effect of these parameters needs to be explored through simulation. Also, while most antenna patterns are fairly smooth and do not exhibit discontinuities, the implicit window introduced when the data is segmented in azimuth does introduce discontinuities. As seen with the linear FM chirp, the discontinuities have the potential of introducing significant errors into the approximation.

6.2.2 Simulations

The purpose of the simulation is to numerically determine the effect of design parameters on the POSP approximation errors. This is accomplished by starting with a base configuration and varying one of the parameters to determine the resulting effect on the POSP approximation errors. The analysis is restricted to the errors in the phase of the frequency domain signal.

The simulator generates the SAR signal observed for a SAR system moving along a perfectly linear trajectory. The relevant parameters of the base configuration used in the comparison are

1. Target slant range of closest approach (SRCA) - 500m

2. Range chirp bandwidth - 200 MHz

3. Carrier frequency - 500 MHz

4. Antenna beamwidth - 16°

We chose to use a standard sinc function antenna pattern

$$\frac{\sin(B\sin\theta)}{B\sin\theta}, \tag{6.26}$$

where B is chosen to yield the appropriate beamwidth, and the signal is oversampled in the azimuth direction to avoid introducing significant errors due to aliasing. For the examples with a 16° beamwidth, the signal is oversampled in the azimuth direction by approximately a factor of 7 which is reduced to a factor of about 2.5 for the 45° beamwidth. Consistent with the assumptions of the previous section, an ideal matched filter is applied to the chirp for each pulse.

The first parameter is the SRCA. The results of the simulation for various values of SRCA are shown in Figure 6.5. As the SRCA increases, the variation in the error as well as the error at dc (zero frequency) decreases. This is consistent with the fact that increasing the SRCA increases the time-bandwidth product of the azimuth chirp. The result suggests that this increase in time-bandwidth product is more significant than the increased error in the time-domain phase approximation. These examples indicate that increasing the minimum SRCA at which targets appear decreases the worst case error in the POSP approximation, and the near range targets in the image are affected more than the far range targets.

The second parameter is the radar carrier frequency. For $f_\rho = 0$, doubling the carrier frequency has precisely the same effect on the time-bandwidth product as doubling the SRCA. The difference is that increasing the carrier frequency increases the bandwidth of the chirp while increasing the SRCA increases the duration of the chirp. Since the only real difference is the chirp rate, one could expect that the improvement in the error should be very similar. This is confirmed in the simulation

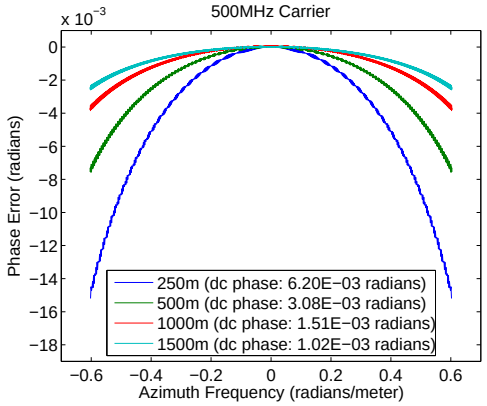

(a) Variation in azimuth frequency, $f_\rho = 0$.

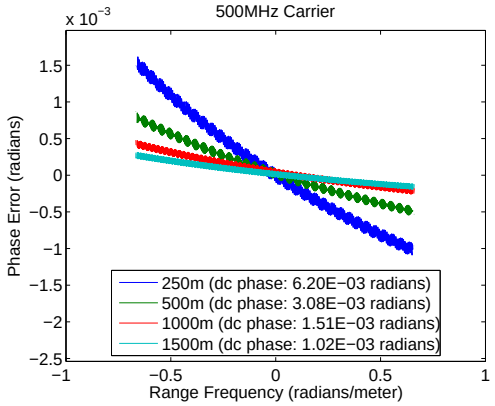

(b) Variation in range frequency, $f_z = 0$.

Figure 6.5: Plots of the frequency domain phase error for simulated targets located at different SRCA. (a) The phase error in azimuth frequency direction. (b) The phase error in range frequency direction. In each case considered, the error variation is reduced with increasing SRCA. This suggests that the increase in time-bandwidth product with increasing SRCA is more significant than the increased error in the approximation of the hyperbolic time-domain phase function.

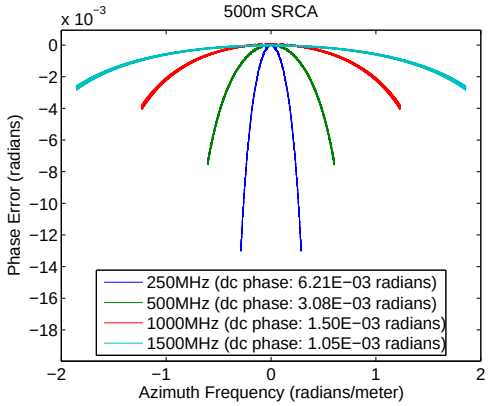

(a) Variation in azimuth frequency, $f_\rho = 0$.

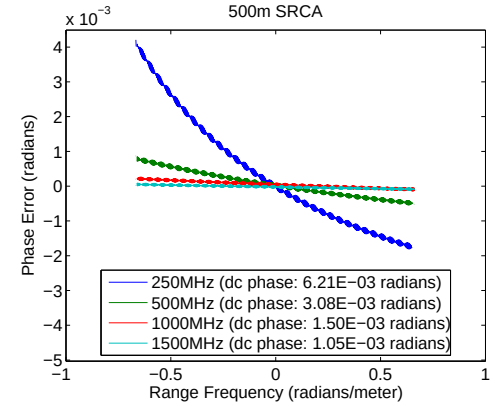

(b) Variation in range frequency, $f_z = 0$.

Figure 6.6: Plots of the frequency domain phase error for SAR systems operating at different carrier frequencies. (a) The phase error in azimuth frequency direction. (b) The phase error in range frequency direction. In each case considered, the error variation is reduced with increasing carrier frequency. This is consistent with the improvement achieved with increasing SRCA. For comparison with Figure 6.5, the green curves are equivalent.

results shown in Figure 6.6(a). The slight discrepancy between the errors in this figure and those in Figure 6.5(a) is presumed to be a caused by the range spreading term (the first term in Equation (6.19)). That term changes when the range to the target changes but does not change with increasing carrier frequency.

Comparing Figure 6.6(b) to Figure 6.5(b), the effect of doubling the carrier frequency does not appear the same as doubling the SRCA. However, in the simulation, the range chirp bandwidth is held constant at 200MHz. The important point is that the range frequency (for which the chirp bandwidth determines the maximum and minimum values) enters into the time-bandwidth product as $(f_\rho + f_{\rho 0})$. At lower carrier frequencies, the variation in time bandwidth product over the chirp bandwidth is more significant. This effect is avoided when the range chirp bandwidth is scaled by the same factor as the radar carrier frequency. Considering the simulated cases in Figure 6.6(b), the difference between the carrier frequency of the green and blue curves is a factor of two, and just considering the center half of the blue curve results in absolute phase errors between about -1e-3 and 1.5e-3 radians. These errors are essentially the same as those observed for the blue curve in Figure 6.5(b).

The third parameter is the antenna beamwidth, and increasing the beamwidth increases both the time and the bandwidth of the signal. The results of the simulation for a few beamwidths is shown in Figure 6.7. As with the other parameters which increased the time-bandwidth product, the POSP approximation errors are reduced as the antenna beamwidth is increased. The high frequency variation also changes; however, this change is attributed to the variation in the magnitude of the discontinuity introduced by the finite length simulation (see Figure 6.8).

The final consideration explored is the effect of segmenting the data. For the simulation, we chose to place the target at 500m and to use a 500MHz carrier frequency. For each window which is simulated, the length of the segment in the along-track dimension is held constant. The three window functions are shown in Figure 6.9(a) where the legend entries designate the location of the right edge of the window with measurements in dB for positions inside the main lobe of the antenna window function. The results of the simulation are shown in Figure 6.9(b) where

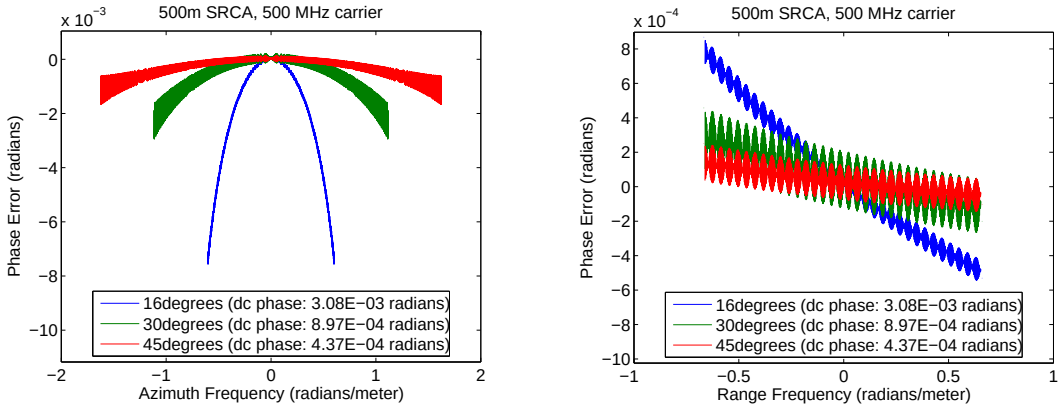

(a) Variation in azimuth frequency, $f_\rho = 0$.

(b) Variation in range frequency, $f_z = 0$.

Figure 6.7: Plots of the frequency domain phase error for SAR systems with different antenna beamwidths. (a) The phase error in azimuth frequency direction. (b) The phase error in range frequency direction. In each case considered, the error variation is reduced with increasing antenna beamwidth.

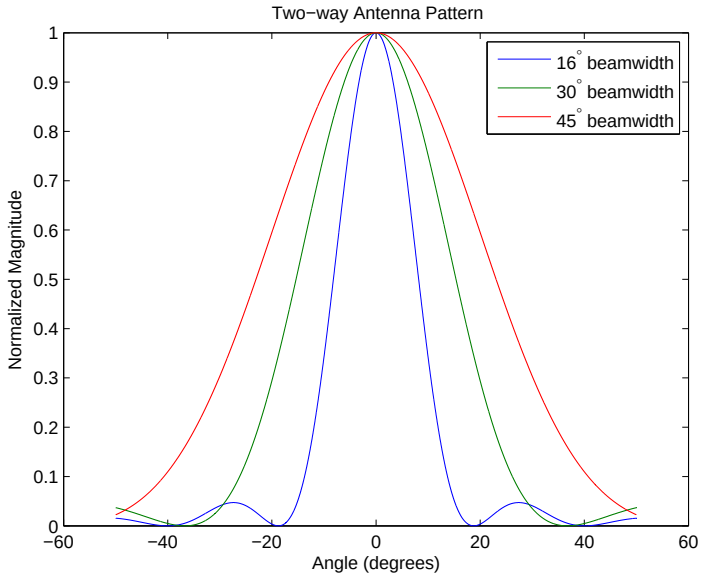

Figure 6.8: Plots of the three normalized antenna patterns used in the simulator. It is presumed that the small discontinuities at the edges are responsible for the higher frequency oscillations in the phase errors shown in Figure 6.7.

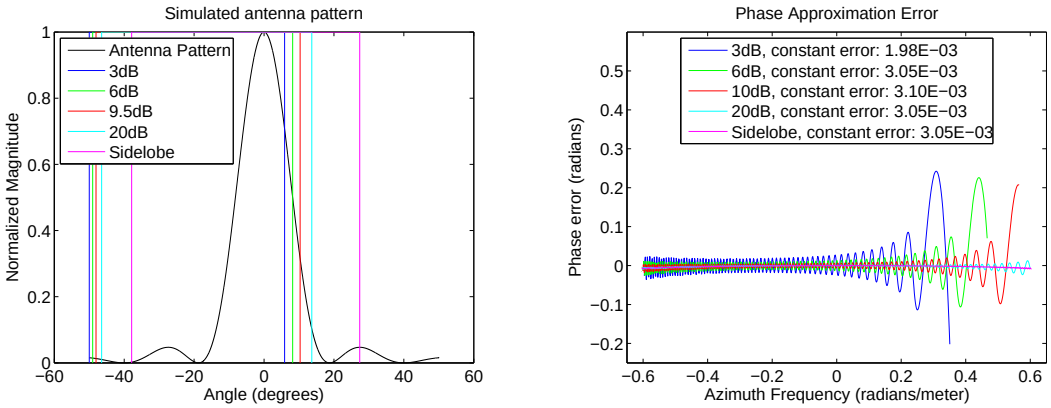

(a) 2-way antenna pattern with applied windows.

(b) POSP approximation phase error.

Figure 6.9: Plots showing the segment processing windows and the associated frequency domain phase errors. The implicit window introduced by segmenting the data in the azimuth direction has the potential of introducing relatively large errors into the POSP approximation.

the constant phase error is approximately the mean error of the oscillations around $f_z = 0$. As expected, a larger discontinuity increases the magnitude of the phase error oscillations. These phase errors are much more significant than those seen earlier.

In summary, the azimuth processing window has the potential of introducing the largest frequency domain phase errors: arriving even to a quarter of a radian. The frequency domain phase errors seen when the azimuth processing window does not introduce significant errors is on the order of 1e-3 radians. For these cases, increasing the antenna beamwidth, the value of $(f_\rho + f_{\rho 0})$, and r all reduce the POSP approximation error. The reduction in frequency domain phase error is attributed to the associated increase in the time-bandwidth product of the signal. Of the cases simulated, the worst case phase error is associated with the 500MHz carrier, the 16° beamwidth, and a 250m SRCA.

6.3 Effects on the Point Spread Function

Having explored the frequency domain phase errors associated with the POSP approximation, the effect of these phase errors on the phase, the peak amplitude, and the shape of the resulting time-domain signal is considered. From the previous analysis, the system parameters which affect the time-bandwidth product have a predictable effect on the frequency domain phase errors. The primary difference is the magnitude of the phase errors. For these reasons, the effect of the frequency domain phase errors is considered for the worst case scenario. The effect of the implicit azimuth window is a little more complex and is explored for three cases.

While increasing the radar carrier frequency, the target's SRCA, and the antenna beamwidth all increased the time-bandwidth product of the signal, the resulting frequency domain phase errors were slightly different. The maximum frequency domain phase error is observed for the case with a 500 MHz carrier, a 16° beamwidth, and a target appearing at 250m. The range and azimuth cuts of the point spread function when the data is focused by the Omega-k algorithm are shown in Figure 6.10. The phase errors reduce the peak magnitude by 0.003 dB, and the 3dB widths in range and azimuth are changed by less than 1/1,000th of a meter. These are not substantial changes.

Concerning the phase of response, the Omega-k algorithm does not compensate for the constant phase term of $\pi/4$ predicted by the POSP approximation. Taking this into account, the un-anticipated phase at the peak is only 1.93e-5 radians. In the range direction, the phase variation across the main lobe is 0.0189 radians, but that is only 0.0005 radians more than the ideal case. In the azimuth direction, the total phase variation across the main lobe is 0.0106 radians. Again, the effect of the frequency domain phase errors is very slight.

The second source of frequency domain phase errors is the implicit window introduced when the signal is segmented in the azimuth direction for processing. The resulting shape of the point spread function for three of the windows is shown in Figure 6.11, and the range and azimuth cuts are shown in Figure 6.12. The peak phase of the response is only slightly affected by the window and the maximum error

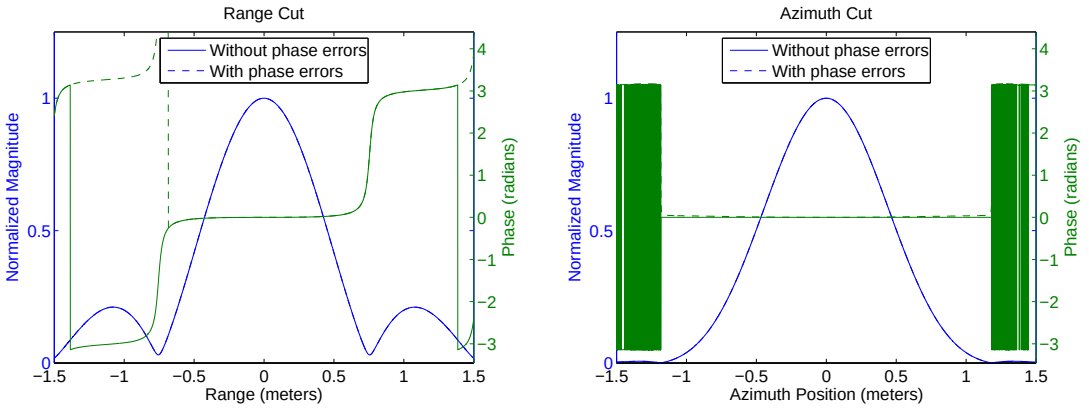

(a) Range cut

(b) Azimuth cut

Figure 6.10: Range and azimuth cuts of the Omega-k focused point spread function for a SAR system with 500MHz carrier, 200MHz range bandwidth, and a 16° beamwidth. This case represents the worst case frequency domain phase errors seen for a low time-bandwidth product in Section 6.2.2. For this configuration, the effect of the frequency domain phase errors is hardly noticeable.

for the three cases is 1.25e-5 radians. The effect of the frequency domain phase errors is most significant for the 3dB window where the diagonal width of the -35dB contour is increased by over 50 percent, the peak magnitude is reduced by 0.35 dB, and the phase variation across the main lobe in the azimuth direction is increased to 0.58 radians.

Even when the frequency domain phase errors are removed, the point spread function is different for the three azimuth windows. The differences between the resulting point spread functions is caused by a change in the support of the signal in the frequency domain. The frequency domain support for two of the window is shown in Figure 6.13. In addition to the effects already seen, the altered support decreases the peak magnitude of the resulting point spread function as shown in Figure 6.14. For the 3dB window, the peak magnitude is attenuated by about 1.4 dB which is much more than the 0.35dB decrease caused by the frequency domain phase errors.

The effect of the frequency domain phase errors on the final point spread function is rather minor. When the azimuth processing window does not substantially

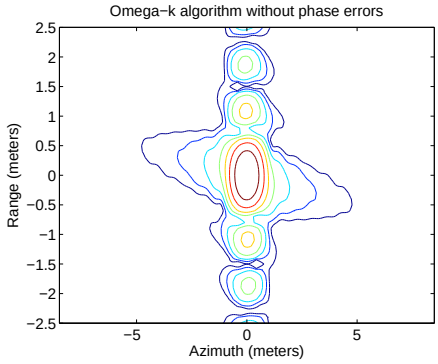

(a) No phase errors, 3dB

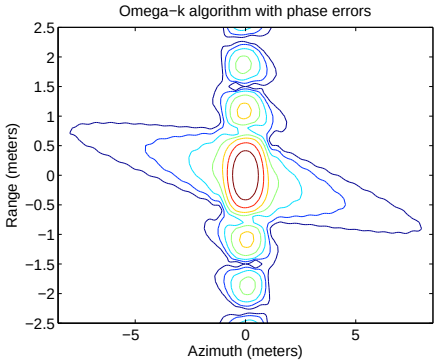

(b) With phase errors, 3dB

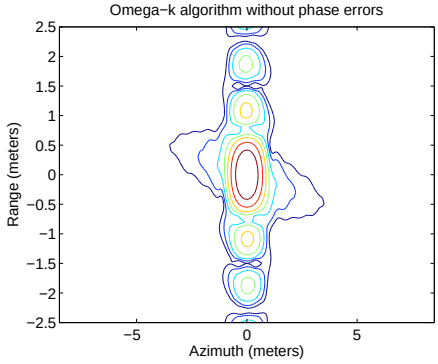

(c) No phase errors, 6dB

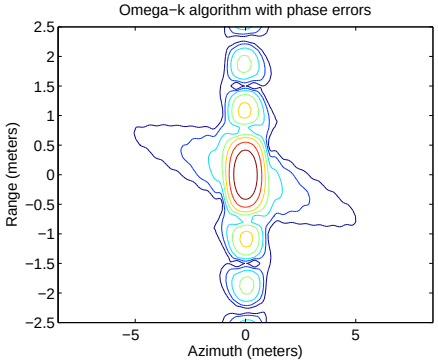

(d) With phase errors, 6dB

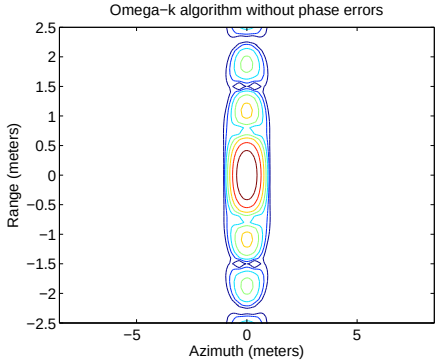

(e) No phase errors, 20dB

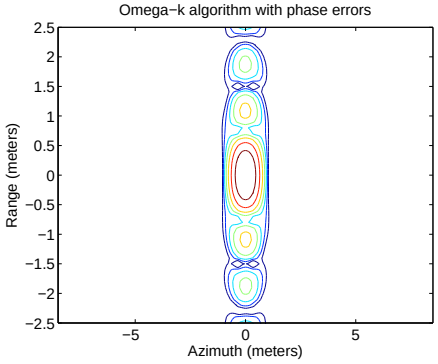

(f) With phase errors, 20dB

Figure 6.11: Contour plots of the point spread functions with contours between -5dB and -35dB at 5dB intervals for three of the five cases in Figure 6.9. For the 3dB and 6dB windows, the frequency domain phase errors stretch out the main lobe diagonally and slightly distort the shape of the range sidelobes. The effect is not noticeable for the 20dB window.

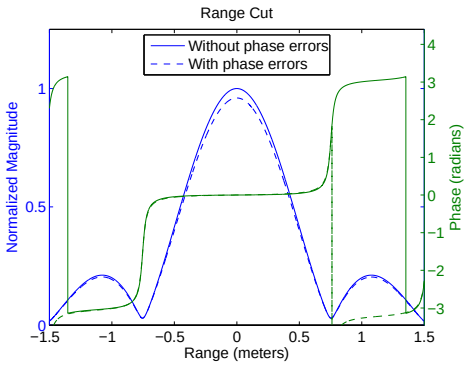

(a) Range Cut, 3dB

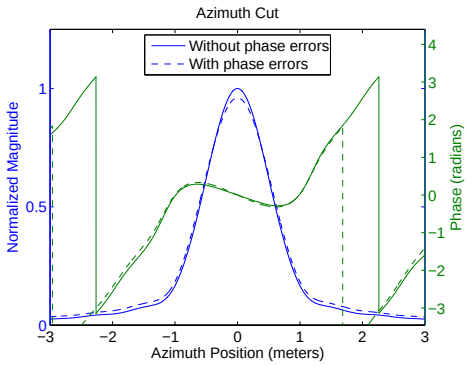

(b) Azimuth Cut, 3dB

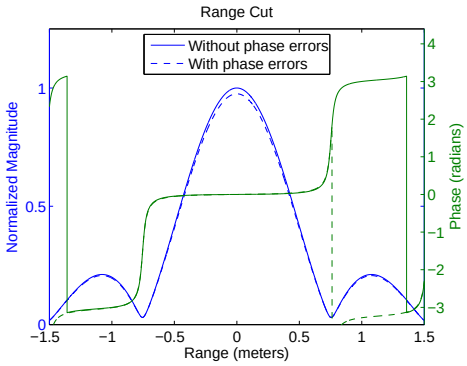

(c) Range Cut, 6dB

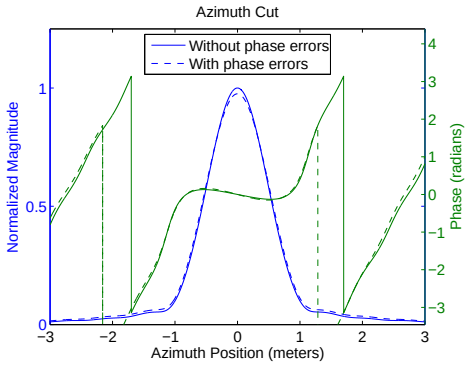

(d) Azimuth Cut, 6dB

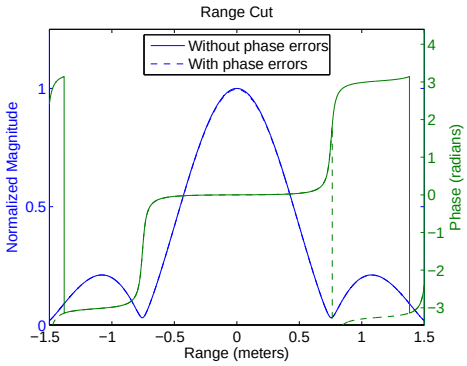

(e) Range Cut, 20dB

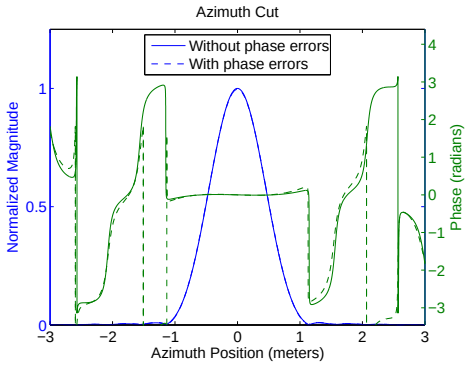

(f) Azimuth Cut, 20dB

Figure 6.12: The range and azimuth cuts of the point spread functions for the cases in Figure 6.11. For the 3dB and the 6dB windows, the frequency domain phase errors decrease the peak magnitude but increase the magnitude where the azimuth sidelobes should be. The phase modulation across the main lobe is slightly increased. These effects are very slight for the 20dB window.

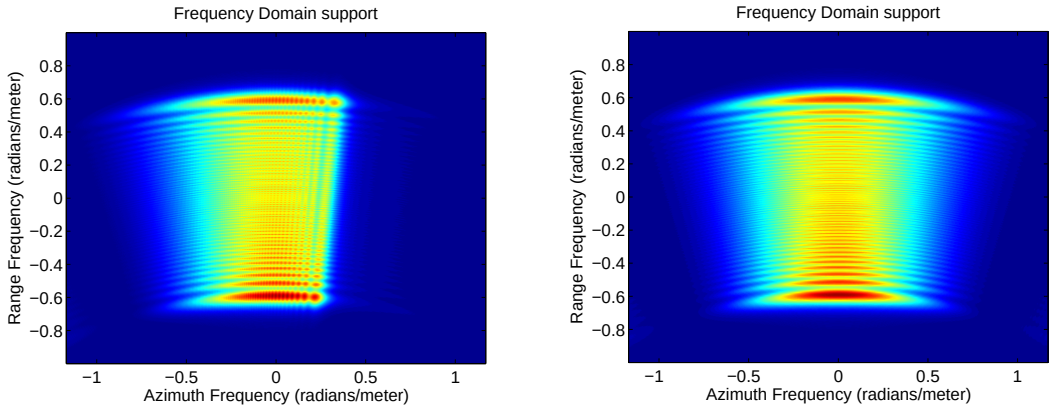

(a) 3dB window

(b) First sidelobe window

Figure 6.13: The magnitude of the Fourier transform for two of the processing windows in Figure 6.9. The 3dB processing window significantly alters the frequency domain support of the SAR signal. The change in frequency domain support alters both the magnitude and the phase of the resulting point spread function. As a note, the variation in the amplitude in the range direction is due to the linear FM range chirp used in the simulation. It is similar to that shown in red in Figure 6.3.

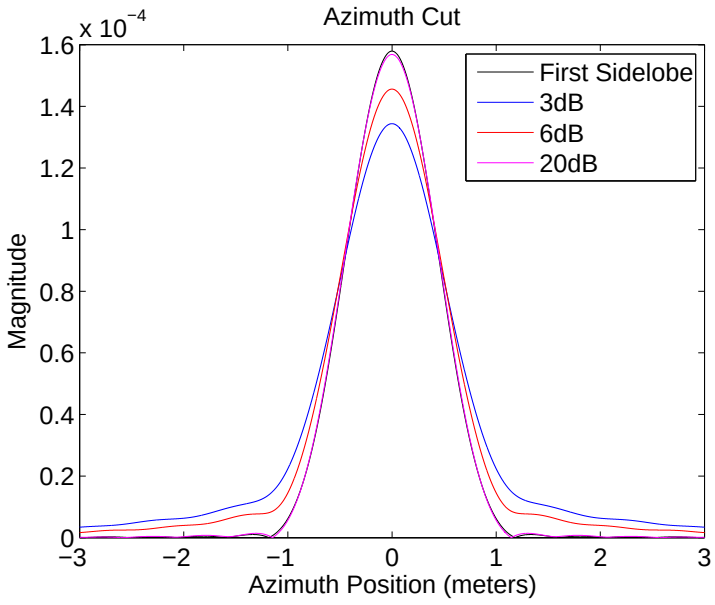

Figure 6.14: The un-normalized magnitude of the azimuth cuts after the frequency domain phase errors are removed for four of the window functions in Figure 6.9. The peak of the point spread function is reduced and the sidelobes disappear as the processing window cuts further into the main lobe of the antenna weighting function. This effect is caused by the altered frequency domain support shown in Figure 6.13.

increase the resulting frequency domain phase errors, the effect of the phase error in the POSP approximation on both the magnitude of the point spread function and the phase across the main lobe is extremely small. Even when the segment window introduces more substantial frequency domain phase errors, the effects of the phase errors are only a fraction of the effect caused by the altered frequency domain support of the signal resulting from the segmentation window.

6.4 Conclusion

The POSP approximation provides a means of obtaining an approximate closed-form expression for integrals without a known closed-form solution. In the context of SAR, the POSP approximation is applied to the azimuth Fourier transform, and the resulting expression is used by the Omega-k algorithm to process the data.

The errors in the frequency domain phase are rather small when the azimuth processing window does not introduce a significant discontinuity into the signal. For the cases considered, the POSP approximation provides an expression for the frequency domain phase which is sufficiently accurate to process the SAR signal. This analysis is limited to broadside SAR systems with sinc-function antenna patterns but can be extended to consider squint-mode SAR systems and systems with other antenna patterns.

The azimuth processing window affects both the frequency domain support of the SAR signal and the accuracy of the POSP approximation. The effect of the altered frequency domain support of the SAR signal has a more significant effect on the resulting point spread function than the frequency domain phase errors. However, their combined effect reduces the peak magnitude of the point spread function by about 2dB when the segment window intersects the antenna window at the 3dB point. This suggests that the angles used in Section 3.2 to identify the valid pixels in a processed SAR image should be larger than those associated with the 3dB point of the antenna window. Using the angle where the antenna window drops to -20dB seems to eliminate most of the undesirable effects.

Chapter 7

Conclusion

This thesis provides a detailed analysis of the Omega-k algorithm. Key aspects of the algorithm are explored both analytically and through numerical simulation. The simulations provide insight into the precise results for specific cases, and the analytical development provides a means for extending the results to new cases.

7.1 Contributions

My contributions to the topic of SAR processing are the following:

- I develop the equations which identify the usable region of a processed SAR image for algorithms which focus target energy to the image location corresponding to the target's zero-Doppler position and slant range of closest approach.
- I present a modification to the Omega-k algorithm which enables the algorithm to achieve a SNR equivalent to that achieved by an ideal matched filter.
- I explore the effects of Stolt mapping on the focused point spread function and discuss how these effects alter the potential interference between nearby scatterers.
- I present the necessary steps for implementing the Omega-k algorithm in discrete time, and I compare two methods for preparing the frequency domain SAR signal for interpolation.
- I investigate the POSP approximation used in the Omega-k algorithm and show that it is accurate for the worst case phase errors observed for a number of SAR configurations.

- I investigate the effect of the azimuth processing window on targets located near the edge of the processing window.

7.2 Future Work

While this thesis provides a detailed look at key aspects of the Omega-k algorithm, it is not comprehensive, and there are additional areas that could be explored.

The first area concerns the scope of this thesis. The work in this thesis is primarily concerned with the application of the Omega-k algorithm to broadside SAR data. Extending the analysis of the POSP approximation errors to squint-mode SAR systems is an important step towards fully understanding the accuracy of the Omega-k algorithm. The effect of the Stolt mapping on squint-mode SAR data should also be addressed.

In terms of implementing the Omega-k algorithm, additional research into the necessary accuracy of the frequency domain interpolation kernel should be performed. While sinc function interpolation is the most accurate approach, it requires a significant amount of computational effort. Investigations into the effect of using non-ideal interpolation kernels provide a means of trading accuracy for efficiency.

Another topic of interest is the effect of frequency domain window functions. These window function are typically used to reduce the sidelobe amplitude of the point spread function. While window functions could be applied separately in the azimuth and range directions, the frequency domain support of the focused SAR signal is not separable in the two dimensions, and the precise effect of frequency domain window functions is unclear. Additional research is needed to understand appropriate methods for applying frequency domain window functions to SAR data processed with the Omega-k algorithm.

Finally, motion compensation is very important for airborne SAR systems. In [12], a modified version of the Omega-k algorithm is developed to compensate for the effects of non-ideal motion. Additional research aimed at understanding and implementing this algorithm is needed to advance the work here at BYU.

Bibliography

[1] I. G. Cumming and F. H. Wong, *Digital Processing of Synthetic Aperture Radar Data*. Artech House, 2005. 1, 31, 45, 51, 53, 57, 58, 59, 66, 67, 93

[2] M. Soumekh, *Synthetic Aperture Radar Signal Processing with MATLAB Algorithms*. John Wiley & Sons, Inc., 1999. 1, 51, 53, 59

[3] J. C. Curlander and R. N. McDonough, *Synthetic Aperture Radar*. John Wiley & Sons, Inc., 1991. 1, 59

[4] D. Thompson, D. Arnold, D. Long, G. Miner, T. Karlinsey, and A. Robertson, "YSAR: a compact, low-cost synthetic aperture radar," *Geoscience and Remote Sensing, 1997. IGARSS '97. Remote Sensing - A Scientific Vision for Sustainable Development., 1997 IEEE International*, vol. 1, pp. 386–388 vol.1, Aug 1997. 1

[5] D. Thompson, D. Arnold, and D. Long, "YINSAR: a compact, low-cost interferometric synthetic aperture radar," *Geoscience and Remote Sensing Symposium, 1999. IGARSS '99 Proceedings. IEEE 1999 International*, vol. 1, pp. 598–600 vol.1, 1999. 1

[6] M. I. Duersch, "BYU micro-SAR: A very small, low-power LFM-CW synthetic aperture radar," Master's thesis, Brigham Young University, 2004. 1

[7] C. Cafforio, C. Prati, and F. Rocca, "SAR data focusing using seismic migration techniques," *Aerospace and Electronic Systems, IEEE Transactions on*, vol. 27, no. 2, pp. 194–207, 1991. 1, 31

[8] A. Potsis, A. Reigber, E. Alivizatos, A. Moreira, and N. K. Uzunoglou, "Comparison of chirp scaling and wavenumber domain algorithms for airborne low-frequency sar," F. Posa, Ed., vol. 4883, no. 1. SPIE, 2003, pp. 11–19. [Online]. Available: http://link.aip.org/link/?PSI/4883/11/1 1

[9] I. Cumming, Y. Neo, and F. Wong, "Interpretations of the omega-k algorithm and comparisons with other algorithms," *Geoscience and Remote Sensing Symposium, 2003. IGARSS '03. Proceedings. 2003 IEEE International*, vol. 3, pp. 1455–1458, July 2003. 1

[10] T. Scheuer and F. Wong, "Comparison of sar processors based on a wave equation formulation," *Geoscience and Remote Sensing Symposium, 1991. IGARSS '91. Remote Sensing: Global Monitoring for Earth Management., International*, vol. 2, pp. 635–639, Jun 1991. 1

[11] R. Bamler, "A comparison of range-doppler and wavenumber domain sar focusing algorithms," *Geoscience and Remote Sensing, IEEE Transactions on*, vol. 30, no. 4, pp. 706–713, Jul 1992. 1, 31

[12] A. Reigber, E. Alivizatos, A. Potsis, and A. Moreira, "Extended wavenumber-domain synthetic aperture radar focusing with integrated motion compensation," *Radar, Sonar and Navigation, IEE Proceedings* -, vol. 153, no. 3, pp. 301–310, June 2006. 86

[13] D. C. Munson and R. L. Visentin, "A signal processing view of strip-mapping synthetic aperture radar," *Acoustics, Speech, and Signal Processing, IEEE Transactions on*, vol. 37, no. 12, pp. 2131–2147, 1989. 5

[14] M. A. Richards, *Fundamentals of Radar Signal Processing.* McGraw-Hill, 2005. 6, 7, 8

[15] A. V. Oppenheim and A. S. Willsky, *Signals and Systems.* Prentice Hall, 1997. 8

[16] D. G. Thompson, "Innovative radar interferometry," Ph.D. dissertation, Brigham Young University, 2001. 14

[17] R. H. Stolt, "Migration by fourier transform," *Geophysics*, vol. 43, no. 1, pp. 23–48, 1978. [Online]. Available: http://link.aip.org/link/?GPY/43/23/1 32

[18] S. Madsen, "Motion compensation for ultra wide band SAR," *Geoscience and Remote Sensing Symposium, 2001. IGARSS '01. IEEE 2001 International*, vol. 3, pp. 1436–1438, 2001. 44

[19] A. V. Oppenheim and R. W. Shafer, *Discrete Time Signal Processing.* Prentice Hall, 1999. 49

[20] A. Papoulis, *Signal Analysis.* McGraw-Hill, Inc., 1977. 60, 67, 89

[21] I. S. Gradshteyn and I. M. Ryzhik, *Table of Integrals, Series, and Products*, 4th ed., A. Jeffrey, Ed. Academic Press, Inc., 1965. 60

Appendix A

Azimuth Fourier Transform

The principle of stationary phase is a method used to arrive at a closed form expression for integrals without a known closed form solution [20]. The approximation is analyzed in detail in Chapter 6; however, all of the steps in the derivation of the azimuth Fourier transform of the SAR signal are not included. These steps are carried out here.

Rearranging the terms in Equation (6.5), the closed form expression for the POSP approximation is

$$\int_a^b f(x)e^{j\lambda g(x)}dx = f(x_{sp})\sqrt{\frac{2\pi}{|\lambda g''(x_{sp})|}}e^{j\lambda g(x_{sp})}e^{\pm j\frac{\pi}{4}}. \tag{A.1}$$

After the range Fourier transform is calculated, the SAR signal (from Equation (2.32)) is

$$\begin{aligned} V(f_\rho, z) &= \frac{k}{\left[(z-z_0)^2+r^2\right]^2} A\left(\frac{z-z_0}{r}\right) H_\rho(f_\rho) \\ &\quad e^{-j2\pi(f_\rho+f_{\rho 0})\sqrt{r^2+(z-z_0)^2}} e^{j\phi_{target}}, \end{aligned} \tag{A.2}$$

where $H(f_\rho)$ is the Fourier transform of $h(\rho)$ and $f_{\rho 0} = 2/\lambda_0$. The azimuth Fourier transform is

$$\begin{aligned} V(f_\rho, f_z) &= kH(f_\rho)e^{j\phi_{target}} \int_{-\infty}^{\infty} \frac{A\left(-\frac{z-z_0}{r}\right)}{\left[(z-z_0)^2+r^2\right]^2} \\ &\quad e^{-j2\pi(f_\rho+f_{\rho 0})\sqrt{(z-z_0)^2+r^2}-j2\pi f_z z}dz. \end{aligned} \tag{A.3}$$

Letting λ in Equation (A.1) be 1, the necessary functions are

$$f(z) = \frac{A\left(-\frac{z-z_0}{r}\right)}{\left[(z-z_0)^2+r^2\right]^2} \tag{A.4}$$

and

$$g(z) = -2\pi(f_\rho + f_{\rho 0})\sqrt{(z-z_0)^2+r^2} - 2\pi f_z z. \tag{A.5}$$

The first derivative of $g(z)$ is

$$\begin{aligned} g'(z) &= -\frac{2\pi(f_\rho + f_{\rho 0})2(z-z_0)}{2\sqrt{(z-z_0)^2+r^2}} - 2\pi f_z \\ &= -\frac{2\pi(f_\rho + f_{\rho 0})(z-z_0)}{\sqrt{(z-z_0)^2+r^2}} - 2\pi f_z, \end{aligned} \tag{A.6}$$

and the second derivative of $g(z)$ is

$$\begin{aligned} g''(z) &= \frac{d}{dz}\left(-\frac{2\pi(f_\rho + f_{\rho 0})(z-z_0)}{\sqrt{(z-z_0)^2+r^2}} - 2\pi f_z\right) \\ &= -\frac{2\pi(f_\rho + f_{\rho 0})}{\sqrt{(z-z_0)^2+r^2}} - \frac{2\pi(f_\rho + f_{\rho 0})(z-z_0)(-\frac{1}{2})2(z-z_0)}{((z-z_0)^2+r^2)\sqrt{(z-z_0)^2+r^2}} \\ &= -\frac{2\pi(f_\rho + f_{\rho 0})}{\sqrt{(z-z_0)^2+r^2}} + \frac{2\pi(f_\rho + f_{\rho 0})(z-z_0)^2}{((z-z_0)^2+r^2)\sqrt{(z-z_0)^2+r^2}} \\ &= \frac{-2\pi(f_\rho + f_{\rho 0})r^2 - 2\pi(f_\rho + f_{\rho 0})(z-z_0)^2 + 2\pi(f_\rho + f_{\rho 0})(z-z_0)^2}{((z-z_0)^2+r^2)\sqrt{(z-z_0)^2+r^2}} \\ &= -\frac{2\pi(f_\rho + f_{\rho 0})r^2}{((z-z_0)^2+r^2)\sqrt{(z-z_0)^2+r^2)}}. \end{aligned} \tag{A.7}$$

At this point, all of the necessary functions have been identified, and the next step is to evaluate them at the stationary phase point.

The stationary phase point is obtained by setting $g'(z)$ equal to zero to yield

$$f_z = -\frac{(f_\rho + f_{\rho 0})(z-z_0)}{\sqrt{(z-z_0)^2+r^2}}, \tag{A.8}$$

and by solving this equation for $(z - z_0)$ to yield

$$(z - z_0) = \pm \frac{f_z r}{\sqrt{(f_\rho + f_{\rho 0})^2 - f_z^2}}. \tag{A.9}$$

The sign ambiguity is resolved by noting that all of the terms on the right side of Equation (A.8) are positive except for $(z - z_0)$. Therefore, the sign of f_z must be the opposite of the sign of $(z - z_0)$. In Equation (A.9), all of the terms except for f_z are positive, and the sign relationship noted for Equation (A.8) is preserved by choosing the negative sign. Therefore, the stationary phase point is

$$z_{sp} = -\frac{f_z r}{\sqrt{(f_\rho + f_{\rho 0})^2 - f_z^2}} + z_0. \tag{A.10}$$

The term $\sqrt{r^2 + (z_{sp} - z_0)^2}$ appears in both $g(z)$ and $g''(z)$. Evaluating that term at the stationary phase point yields

$$\begin{aligned}
\sqrt{r^2 + (z_{sp} - z_0)^2} &= \sqrt{r^2 + \frac{f_z^2 r^2}{(f_\rho + f_{\rho 0})^2 - f_z^2}} \\
&= r\sqrt{1 + \frac{f_z^2}{(f_\rho + f_{\rho 0})^2 - f_z^2}} \\
&= r\sqrt{\frac{(f_\rho + f_{\rho 0})^2 - f_z^2 + f_z^2}{(f_\rho + f_{\rho 0})^2 - f_z^2}} \\
&= \frac{r(f_\rho + f_{\rho 0})}{\sqrt{(f_\rho + f_{\rho 0})^2 - f_z^2}}.
\end{aligned} \tag{A.11}$$

Substituting Equation (A.10) and Equation (A.11) into Equation (A.5) yields

$$\begin{aligned}
g(z_{sp}) &= -\frac{2\pi r(f_\rho + f_{\rho 0})^2}{\sqrt{(f_\rho + f_{\rho 0})^2 - f_z^2}} + \frac{2\pi f_z^2 r}{\sqrt{(f_\rho + f_{\rho 0})^2 - f_z^2}} - 2\pi f_z z_0 \\
&= -\frac{2\pi r(f_\rho + f_{\rho 0})^2 - 2\pi f_z^2 r}{\sqrt{(f_\rho + f_{\rho 0})^2 - f_z^2}} - 2\pi f_z z_0 \\
&= -2\pi r \left[\frac{(f_\rho + f_{\rho 0})^2 - f_z^2}{\sqrt{(f_\rho + f_{\rho 0})^2 - f_z^2}} \right] - 2\pi f_z z_0 \\
&= -2\pi r \sqrt{(f_\rho + f_{\rho 0})^2 - f_z^2} - 2\pi f_z z_0,
\end{aligned} \tag{A.12}$$

which is the 0th order coefficient for the Taylor series representation. Then, inserting Equation (A.10) and Equation (A.11) into Equation (A.7) yields the second order Taylor coefficient

$$\begin{aligned} g''(z_{sp}) &= -2\pi r^2 (f_\rho + f_{\rho 0}) \frac{[(f_\rho + f_{\rho 0})^2 - f_z^2)]^{\frac{3}{2}}}{r^3 (f_\rho + f_{\rho 0})^3} \\ &= -\frac{2\pi}{r} \frac{((f_\rho + f_{\rho 0})^2 - f_z^2)^{\frac{3}{2}}}{(f_\rho + f_{\rho 0})^2}. \end{aligned} \tag{A.13}$$

Finally,

$$f(x_{sp}) = A\left(\frac{f_z}{\sqrt{(f_\rho + f_{\rho 0})^2 - f_z^2}}\right) \frac{((f_\rho + f_{\rho 0})^2 - f_z^2)^2}{r^4 (f_\rho + f_{\rho 0})^4}. \tag{A.14}$$

The first two terms on the right side of Equation (A.1) are

$$\begin{aligned} f(x_{sp}) \sqrt{\frac{2\pi}{|\lambda g''(x_{sp})|}} &= \frac{((f_\rho + f_{\rho 0})^2 - f_z^2)^2}{r^4 (f_\rho + f_{\rho 0})^4} \frac{\sqrt{r}(f_\rho + f_{\rho 0})}{((f_\rho + f_{\rho 0})^2 - f_z^2)^{\frac{3}{4}}} A(M) \\ &= \frac{((f_\rho + f_{\rho 0})^2 - f_z^2)^{\frac{5}{4}}}{r^{\frac{7}{2}} (f_\rho + f_{\rho 0})^3} A(M), \end{aligned} \tag{A.15}$$

where

$$M = \frac{f_z}{\sqrt{(f_\rho + f_{\rho 0})^2 - f_z^2}}. \tag{A.16}$$

Incorporating the rest of the terms in Equation (A.1) yields

$$\frac{((f_\rho + f_{\rho 0})^2 - f_z^2)^{\frac{5}{4}}}{r^{\frac{7}{4}} (f_\rho + f_{\rho 0})^3} A(M) e^{-j2\pi r \sqrt{(f_\rho + f_{\rho 0})^2 - f_z^2} - j2\pi f_z z_0} e^{-j\frac{\pi}{4}}, \tag{A.17}$$

and the azimuth Fourier transform of the SAR signal is

$$\begin{aligned} V(f_\rho, f_z) &= k \frac{((f_\rho + f_{\rho 0})^2 - f_z^2)^{\frac{5}{4}}}{r^{\frac{7}{4}} (f_\rho + f_{\rho 0})^3} A\left(\frac{f_z}{\sqrt{(f_\rho + f_{\rho 0})^2 - f_z^2}}\right) H_\rho(f_\rho) \\ &\quad e^{-j2\pi r \sqrt{(f_\rho + f_{\rho 0})^2 - f_z^2} - j2\pi f_z z_0} e^{-j\frac{\pi}{4}} e^{j\phi_{target}}. \end{aligned} \tag{A.18}$$

Appendix B

Quadrature Demodulation

In radar, signals are almost always complex (i.e. they have both real and imaginary parts). The complex signal is obtained through quadrature demodulation. As this process may be unfamiliar to some readers, an example is provided. This topic is also addressed in [1].

Consider a signal of the form $w(t)cos(2\pi f_0 t + \theta(t))$ where f_0 is the carrier frequency, $\theta(t)$ defines the chirp, and $w(t)$ is a weighted window function which limits the length of the signal. This signal is transmitted from the antenna and an echo is received after a delay τ. In a real system, the signal is also attenuated, however this attenuation is not significant in the following analysis. Ignoring that attenuation, the received signal is $w(t-\tau)cos[2\pi f_0(t-\tau) + \theta(t-\tau)]$. That received signal is turned into a complex signal by an operation known as quadrature demodulation which is expressed as

$$V(t) = w(t-\tau)cos[2\pi f_0(t-\tau) + \theta(t-\tau))[cos(2\pi f_0 t) - jsin(2\pi f_0 t)]. \quad \text{(B.1)}$$

The demodulation process is performed by mixing the received signal separately by the cosine and the negative sine. Then, the signals are low pass filtered and digitized. To this point, the process is identical to that used in communication systems; however, in radar, the two signals are then combined by multiplying the digitized, sine-modulated signal by the imaginary number j and adding the two signals together.

The justification for this process is made clear by simplifying (B.1) as follows:

$$\begin{aligned} V(t) &= w(t-\tau)cos[2\pi f_0(t-\tau)+\theta(t-\tau)][cos(2\pi f_0 t)-jsin(2\pi f_0 t)] \quad \text{(B.2)} \\ &= w(t-\tau)cos[2\pi f_0(t-\tau)+\theta(t-\tau)]e^{-j2\pi f_0 t} \\ &= 0.5w(t-\tau)\left(e^{j2\pi f_0(t-\tau)+j\theta(t-\tau)}+e^{-j2\pi f_0(t-\tau)-j\theta(t-\tau)}\right)e^{-j2\pi f_0 t} \\ &= 0.5w(t-\tau)\left(e^{-j2\pi f_0\tau+j\theta(t-\tau)}+e^{-j4\pi f_0 t+j2\pi f_0\tau-j\theta(t-\tau)}\right). \quad \text{(B.3)} \end{aligned}$$

The second exponential term under the parentheses in (B.3) is removed by the low-pass filter applied prior to digitizing the data. Therefore, the final signal is actually

$$V(t) = 0.5w(t-\tau)e^{-j2\pi f_0\tau}e^{j\theta(t-\tau)}. \quad \text{(B.4)}$$

The first exponential term in (B.4) is just a phase term determined by the echo delay and the radar carrier frequency, and the second exponential term is the actual chirp.